INVESTIGATION OF SMALL SCALE WEAK SOLAR EMISSION FEATURES AT LOW RADIO FREQUENCIES

A thesis submitted towards partial fulfillment of
BS-MS Dual Degree Programme

by

AKSHAY S
Registration No. : 20121045

INDIAN INSTITUTE OF SCIENCE EDUCATION AND RESEARCH PUNE
DR. HOMI BHABHA ROAD,
PASHAN, PUNE - 411008, INDIA.

April 2017

under the guidance of

DIVYA OBEROI

READER-F,
NATIONAL CENTRE FOR RADIO ASTROPHYSICS-
TATA INSTITUTE OF FUNDAMENTAL RESEARCH,
PUNE UNIVERSITY CAMPUS,
POST BAG 3, GANESHKHIND, PUNE - 411007, INDIA

Certificate

This is to certify that this thesis entitled "Investigation of Small Scale Weak Solar Emission Features at Low Radio Frequencies" submitted towards the partial fulfillment of the BS-MS dual degree programme at the Indian Institute of Science Education and Research Pune represents original research carried out by Akshay S at the National Centre for Radio Astrophysics-Tata Institute of Fundamental Research, Pune under the supervision of Divya Oberoi during the academic year 2016-2017.

Student
AKSHAY S

Supervisor
DIVYA OBEROI

Thesis Advisory Committee:
DIVYA OBEROI
PRASAD SUBRAMANIAN

This thesis is dedicated to my parents.

Declaration

I hereby declare that the matter embodied in the report entitled "Investigation of Small Scale Weak Solar Emission Features at Low Radio Frequencies" are the results of the investigations carried out by me at the National Centre for Radio Astrophysics-Tata Institute of Fundamental Research, Pune under the supervision of Divya Oberoi and the same has not been submitted elsewhere for any other degree.

Student
AKSHAY S

Supervisor
DIVYA OBEROI

Acknowledgements

I would like to firstly thank my advisor Divya Oberoi for his continued guidance over the course of this project. He was willing to give me the space to explore and implement my own ideas, while at the same time providing useful suggestions during crucial periods of this research work. I also thank my group members, Atul Mohan and Rohit Sharma (both graduate students at NCRA-TIFR, Pune) for their timely help and advice. In addition, I would like to acknowledge our project collaborators Victor Pankratius and Colin Lonsdale (both affiliated to MIT Haystack Observatory, USA) for their valuable contributions towards the completion of this work. I would also like to give a special mention to the Murchison Widefield Array team for the hard work put in towards collecting the data analyzed in this work. I thank the Kishore Vaigyanik Protsahan Yojana for the financial support provided during the course of this work. Finally, I owe a deep debt of gratitude towards my parents for comforting me with years of unending emotional and financial support.

Abstract

Solar observations at low radio frequencies using the Murchison Widefield Array have recently revealed the presence of a myriad of weak, short-lived and narrow-band emission features, even during quiet and moderately active solar conditions. In terms of their appearance in the time-frequency plane, these features are quite unlike any of the known classes of radio bursts and their detailed observational characteristics are yet to be established. They occur at rates of a few thousands per hour in the 30.72 MHz observational bandwidth and hence, necessarily require an automated approach for their characterization. Here, we develop a wavelet-based pipeline using a 2D Ricker wavelet for automated feature recognition from the dynamic spectrum. We perform separate non-imaging and imaging studies of these features to investigate distributions of their peak flux densities, energies, morphologies in the dynamic spectrum, source sizes and locations, and search for their associations with known solar active regions. We find the typical radiated energies associated with these features to be about $10^{15} - 10^{18}$ ergs, placing them amongst the weakest radio bursts reported in literature. The distribution of their peak flux densities is well-fit by a power law with index -2.23 over the $12 - 155$ SFU range, implying that they can contribute to coronal and chromospheric heating in an energetically significant manner. Images of a small subset of these features reveal the presence of two bright, compact, extended sources. While one of these two sources appears only during the occurrence of some features, the other source is persistently present, even during feature-less regions of the dynamic spectrum. The presence of this persistent source together with its association to a flaring region observed at EUV wavelengths suggest that the observed small-scale features correspond to type-I bursts embedded in a type-I storm. Analogous to type-I bursts, these features appear to ride on a variable, enhanced, broadband continuum, and possess short spectral and temporal spans of about $4 - 5$ MHz and $1 - 2$ seconds respectively. A 2D Gaussian model is found to serve as a powerful tool to track the locations and morphologies of their sources with an accuracy better than the intrinsic resolution of the observing instrument.

Contents

List of Figures

List of Tables

Chapter 1

Introduction

The radio Sun is extremely dynamic, exhibiting a large variety of phenomena spanning a large range of spatial and temporal scales. Over the last 70 years, radio astronomers have enthusiastically developed novel techniques and instruments to study the Sun. At high frequencies (optical, EUV and X-ray), electromagnetic emission from the Sun is dominated by blackbody emission from the optically thick photosphere. At these frequencies, the corona and the chromosphere are practically transparent. However, at radio frequencies ($\lesssim$ 10 GHz), solar emission arises primarily from the corona and chromosphere, and is produced via three different mechanisms namely[1]:

1. **Thermal bremsstrahlung (free-free emission) from Coulomb collisions between electrons in the solar coronal plasma with temperature of about 2×10^6 K :**
   This emission is purely thermal in nature and is expected to be ubiquitous over the solar surface. It is observed to exist at all times, even during solar minima (minimum of the empirically observed 11-year cycle in solar magnetic activity) when magnetic field enhancements such as sunspots and active regions are absent on the solar surface. It, hence, forms the minimum baseline solar flux detectable at any time and is generally referred to as the "quiet Sun" emission.

2. **Gyrosynchotron emission from mildly relativistic electrons in the solar corona :**
   Unlike the quiet Sun emission, this emission, produced by the random-phase gyromotion of electrons in the solar corona, is most efficient in strong magnetic fields and is hence, closely tied to sunspots and active regions.

3. **Plasma emission at the local plasma frequency and its harmonics :**
   This emission is purely non-thermal in nature and is a characteristic of the disturbed Sun. It generally results as a consequence of kinematic instabilities generated in the solar corona through the production of unstable particle distributions by bursty magnetic reconnection processes.

At low radio frequencies ($\lesssim$ 1 GHz), gyrosynchrotron emission gets self-absorbed in the corona and hence, free-free emission and plasma emission dominate the solar radiation. While free-free emission and gyrosynchrotron emission are continuum processes and are incoherent in nature, plasma emission is a coherent emission mechanism. The concept of "brightness temperature" is commonly used in radio astronomy to distinguish between coherent and incoherent emission mechanisms.

1.1 Brightness temperature as a tool to identify coherent emission mechanisms

The brightness temperature (T_b) of a source is defined as the temperature of a blackbody which, when in thermal equilibrium with its surroundings, produces the same brightness distribution as the source. For a source producing brightness B_ν at radio frequency ν, the corresponding brightness temperature is given by[2]:

$$T_b = \frac{B_\nu c^2}{2k_b \nu^2} \tag{1.1}$$

where c is the speed of light in vacuum and k_b is the Boltzmann constant. T_b corresponds to the temperature of the radiation and does not represent the physical temperature of the source unless the source brightness distribution is thermal. Therefore, the expected brightness temperature for the purely thermal free-free emission equals the electron temperature in the solar corona and is of order 10^6 K.

The observational signature of a coherent emission process is a brightness temperature that is too large to be explained by any incoherent emission mechanism[3]. The coherent nature of plasma emission ($T_b \approx 10^8 - 10^{12}$ K) from the solar corona can then give rise to large observational signatures for intrinsically small electromagnetic wave energies. This makes the low radio frequency band of the electromagnetic spectrum a promising regime for the observation and characterization of signatures of coronal plasma emission.

Plasma emission from the solar corona manifests itself in the form of non-thermal, sporadic radio bursts of short time scales (of order seconds to minutes) at the local plasma frequency (ν_p) or its first harmonic. As ν_p scales as the square root of the local electron density in a plasma, given a coronal electron density profile, electromagnetic emission via plasma emission processes at the local plasma frequency or its harmonic serves as a marker to track the height of emitting plasma in the solar corona. In solar physics, dynamic spectra (DS) which trace the evolution of the received solar spectra with time are often used to identify and distinguish between different kinds of solar radio bursts. Ignoring the several small-scale density inhomogeneities present in the solar corona, the coronal electron density profile $n_e(r)$ falls off monotonically with the radial coordinate r (measured from the centre of the Sun). In such a scenario, ν_p decreases with increasing r and hence, a radio burst with negative frequency drift rate ($d\nu/dt$) in the DS corresponds to a blob of plasma moving outwards from the corona into interplanetary space.

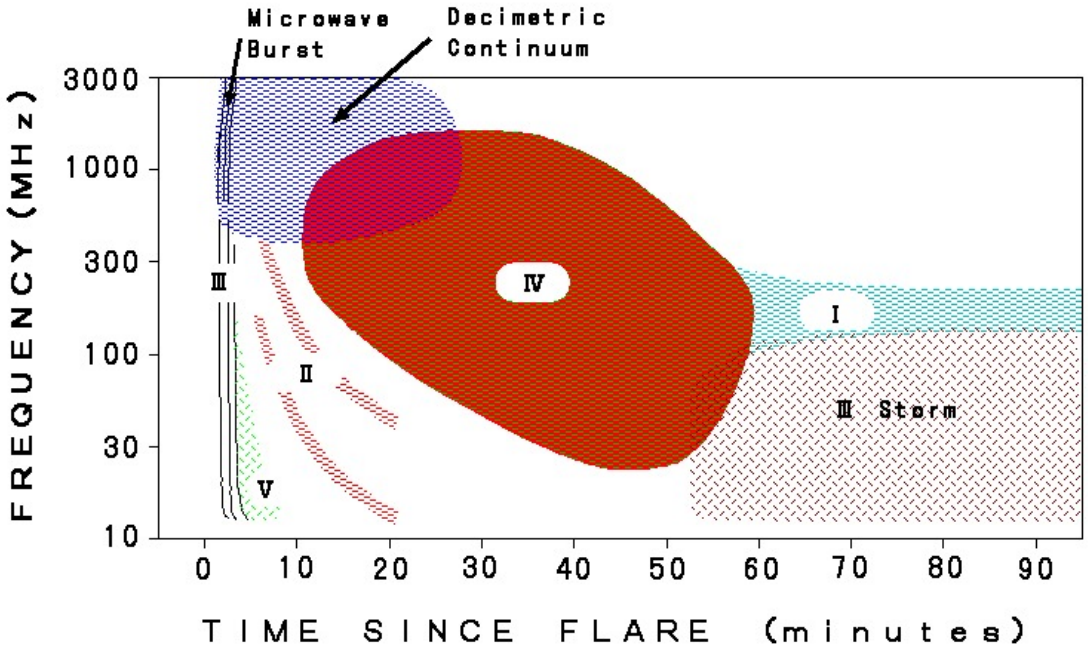

Figure 1.1: A dynamic spectrum showing different classes of solar radio bursts that have been well-studied and characterized in literature.
Image credits : `http://sunbase.nict.go.jp/solar/denpa/hiras/types.html`

1.2 Classes of solar radio bursts

Figure 1.1 shows an example solar DS illustrating different types of solar metric radio bursts. On the basis of their appearance in the solar DS, these bursts are classically classified into five types :

1. **Type-I bursts :**
   These appear in the DS as stationary bursts with short durations (of order a second) and narrow bandwidths ($\lesssim$ 10 MHz). Quite often, in events called type-I storms, type-I bursts are found embedded on top of a broadband continuum at rates as high as one per second. Such type-I storms typically last for several hours to days. As of today, the exact mechanism behind type-I storm production (also called radio noise storms) is still unknown but it is believed to be associated with continuous magnetic reconnection above active regions. Observations of type-I storms suggest that type-I bursts are produced through plasma emission at ν_p with no harmonic counterpart [4].

2. **Type-II bursts :**
   Type-II bursts are slow-drifting bursts of plasma emission that typically last for about 3-30 minutes and are often observed with structure at both ν_p and its first harmonic. Historically, the occurrences of these bursts have been found to be well-correlated with that of coronal mass ejections (CMEs) [5]. Due to this association, it is currently accepted that the cause of a type-II burst is a shock wave propagating outwards from the solar

corona into the interplanetary space at speeds of about $200 - 2000$ kms^{-1}.

3. **Type-III bursts :**
   Type-III bursts are rapidly drifting bursts ($|d\nu/dt| \approx 300 - 1000$ MHz/s) of plasma emission. These bursts are associated with the propagation of a relativistically propagating (speed of about c/3 in the lower corona) beam of plasma through the solar corona. The currently accepted theory of type-III production was first put forward by Ginzburg and Zhelenzniakov in 1958. According to their theory, a type-III burst is produced as a result of a two-stream instability of an electron beam. This instability is generated by the impingement of an accelerated population of electrons upon a cooler thermal population of electrons. This bump-on-the-tail instability then gives rise to Langmuir waves at the local plasma frequency [6, 7]. Nonlinear wave-wave interactions between Langmuir waves and ion sound waves ultimately lead to the production of electromagnetic emission at ν_p and its first harmonic. Quite often, type-III bursts are observed to drift from high frequencies to low frequencies, corresponding to an electron beam propagating outwards from the corona. However, reverse slope type-III bursts have also been occasionally observed.

4. **Type-IV bursts :**
   Type-IV bursts can be either stationary or moving. Stationary type-IV bursts are characterized by a broadband continuum that lasts for several hours to days. These bursts are sometimes highly polarized and are produced either via plasma emission (circularly polarized) or gyrosynchrotron emission (x-mode polarized) emitted by non-thermal electrons trapped in flare loop geometries. Moving type-IV bursts are produced in a similar manner when these electrons are either trapped in eruptive prominences or are entrenched in a CME.

5. **Type-V bursts :**
   These bursts typically form a smooth, short-lived (~1-3 minutes) continuum that follows a type III burst and are generally x-mode polarized (opposite to that of the associated type-III burst). They are never found in isolation and are believed to be a by-product of the passage of the slower type-III electrons along diverging magnetic field line geometries, with both forward and counter-streaming Langmuir waves generated by the previous passage of type-III electrons.

Just like the classical metric radio bursts discussed above, there exist a variety of decimetric radio bursts [1] that comprise the decimetric continuum shown in Fig. 1.1. However, details of these bursts are beyond the scope of this work and shall not be discussed here. As type-I and type-III bursts are the two classes of bursts most relevant to this work, their properties have been summarized in Table 1.1.

Table 1.1: Summary of observational characteristics of solar type-I and type-III bursts. Content courtesy : http://www.sws.bom.gov.au/Category/World%20Data%20Centre/Data%20Display%20and%20Download/Spectrograph/Solar%20Radio%20Burst%20Classifications.pdf

Type	Characteristics	Duration	Frequency range	Associated phenomena
I	Short-lived, narrow-band bursts. Usually occur in large numbers with underlying continuum.	Single burst: 1s Storm: hours−days	80−200 MHz	Active regions, flares, eruptive prominences.
III	Fast drifting bursts. Can occur in isolation, in groups or storms. Can display structure at first harmonic.	Single burst: 1−3 s Group: 1−5 min. Storm: minutes−hours	10 kHz−1 GHz	Active regions, flares.

1.3 Recent discovery using new generation instruments

New generation radio arrays such as the Low-Frequency Array (LOFAR) in Europe, the Murchison Widefield Array (MWA) in Australia and the Long Wavelength Array (LWA) in New Mexico, USA have recently revealed the presence of previously unappreciated diversity and complexity in non-thermal solar emission features at low radio frequencies [8, 9, 10]. The MWA is a low frequency radio interferometer that operates in the frequency range from $80-300$ MHz. It is a precursor to the Square Kilometre Array-Low (SKA-Low) and is situated at the Murchison Radio Observatory in Western Australia. This area is extremely sparsely populated and is hence, suitable for radio astronomical observations due to exceptionally low levels of radio frequency interference (RFI) from sources commonly associated with communications technology and human lifestyle. The dominant sources of RFI in these regions are radio waves from satellites, along with the RFI reflected off aircraft.

The MWA [11, 12, 13]comprises of 2048 dual polarization dipoles arranged as 128 tiles where each tile is a 4×4 array of dipoles. Each dipole is sensitive to two instrumental polarizations - X (east-west) and Y (north-south) along its two perpendicular arms. Figure 1.2 shows the structure of a single MWA tile. A tile forms the basic antenna element of the MWA. A pair of tiles constitute a single two-element interferometric baseline of the MWA. As the MWA consists of 128 tiles, the total number of baselines in the MWA is 8128 ($=^{128} C_2$). While a large number (112) of these tiles are distributed within a circular core region of radius 750 m, a few of them are scattered at distances beyond 750 m from the centre of the array. The length of the longest baseline in the MWA is about 3 km. The properties and observational capabilities of the MWA are summarized in table 1.2. As compared to conventional "sweep type"

Figure 1.2: A typical MWA tile consisting of 16 phased dipoles.
Image credits : `http://www.caastro.org/news/tingay-et-al-pasa-2013`

Table 1.2: Properties and observational capabilities of the MWA.
Content courtesy : `http://mwatelescope.org/telescope`

Frequency range	80 - 300 MHz
Number of receptors	2048 dual polarization dipoles
Number of antenna tiles	128
Number of baselines	8128
Collecting area	Approx. 2000 sq. meters
Field of view	Approx. 15 - 50 deg. (200 - 2500 sq. deg.)
Instantaneous bandwidth	30.72 MHz
Spectral resolution	40 kHz
Temporal resolution	0.5 seconds
Polarization	Full Stokes (I, Q, U, V)
Array configuration	50 antenna tiles within 100 m 62 antenna tiles between 100 m and 750 m 16 antenna tiles at 1500 m

spectrometers that scan a sub-band of the observing bandwidth of a DS at one instant of time and then move to an adjacent sub-band of the same DS at the next instant, the FFT spectra used by the MWA and other new generation radio arrays offer the capability to scan the entire DS bandwidth instantaneously.

The design of the MWA and its radio quiet environment together with the radio advantage offered by the coherent nature of plasma emission make it an excellent choice as an instrument for observation and characterization of previously undetected varieties of solar radio bursts. The significant sensitivity advantage provided by the FFT spectrograph coupled with the frequency (40 kHz) and time resolution (0.5 s) of the MWA solar DS has revealed the presence of a large number of weak, short-lived and narrow-band emission features, even during what are conventionally regarded as quiet to moderately active solar conditions.

In terms of their morphology in the MWA DS, these non-thermal features resemble miniature versions of solar type-III bursts, with spectral and temporal spans of about a few MHz and a second respectively. Previous radio imaging studies[9] of such features have shown that their brightness temperatures are similar to those observed for type-III bursts, implying a coherent emission mechanism behind their production. The apparently ubiquitous presence of these features raises the likelihood that they might correspond to observational signatures of nanoflares which were hypothesized by Eugene Parker in 1988 as a possible solution to the coronal heating problem [14].

1.3.1 Coronal heating problem and the nanoflare hypothesis

The coronal heating problem has been one of many unresolved problems in astrophysics for several decades. The heat generated during nuclear fusion in the Sun flows outwards from its core to its surface and then into its corona from where it is dissipated into interplanetary space. However, while the temperature of the photosphere is about 6000 K, the temperature of the solar corona, as estimated through observations at metre and centimetre wavelengths, is as high as 2×10^6 K. This apparent violation of the Second Law of Thermodynamics suggests the presence of a heating mechanism to compensate for energy losses primarily due to radiation from the corona. According to Parker's theory, the solar corona is continuously heated by the occurrence of a large number of microscopic flaring events called nanoflares [14]. These are considered to be miniature versions of solar flares with an energy budget of $10^{24} - 10^{27}$ ergs (about $10^{-9} - 10^{-6}$ times that of the largest solar flares), corresponding to thermal emission at EUV / X-ray wavelengths. They are believed to occur ubiquitously over the solar surface, even during quiet solar conditions and are expected to lead to coronal heating via small-scale magnetic reconnection processes. At low radio frequencies, the dominant mode of emission expected from nanoflares is plasma emission.

The observed characteristics of the small-scale features of interest in the MWA DS make them suitable candidates for being radio signatures of nanoflares. However, in order for these features to contribute effectively to coronal and chromospheric heating, the power law ($dN/d\mathscr{W} \propto \mathscr{W}^{\alpha}$) index α, of flare energies ($\mathscr{W}$) is required to satisfy the criterion $\alpha \leq -2$ [15]. Some of the known classes of radio bursts do satisfy this requirement. Type-I bursts are reported to follow a power law with index $\alpha \approx -3$ [16]over a peak flux density range of 20-3000 SFU [1]. Type-III bursts, on the other hand, are found to obey a power law distribution of peak fluxes over the flux range $10^2 - 10^4$ SFU with a power law index $\alpha \approx -1.7$ [17]. As the presence of small-scale solar emission features in the MWA DS has been established comparatively recently only [9], their detailed observational characteristics in terms of distributions of their spectral and temporal widths, energy content, slopes in the frequency-time plane, distributions over the solar disk

[1] SFU stands for Solar Flux Units. 1 SFU $= 10^4$ Jy $= 10^{-22}$ Wm^{-2}Hz^{-1}.

and associations with active regions are yet to be determined. Such a statistical characterization of their properties would be the first step towards understanding them and evaluating their potential for coronal heating.

However, the small-scale features of interest occur at rates as high as a few thousands per hour in the 30.72 MHz MWA DS bandwidth. This necessitates an automated approach for their recognition from the DS. In this work, we develop a wavelet-based approach for automated feature detection from the DS, and perform separate non-imaging and imaging studies for their detailed characterization.

Chapter 2

Methodology

2.1 Observing Plan

The data analyzed in this work were collected using the MWA on August 31, 2014 between 00:32:00 UTC and 06:56:00 UTC as part of the solar observing proposal G0002. According to the SWPC event list and the NOAA Active Region Summary (`http://www.solarmonitor.org`) for this day, this observing period was marked by medium levels of solar activity. At X-ray wavelengths, solar activity during a given interval of time is measured in terms of the number of X-ray solar flares observed during that interval. On the basis of their energy content in the wavelength range 1-8 Å, X-ray flares are classified, in order of increasing X-ray brightness, as : A, B, C, M and X. Each letter in this scheme represents a 10-fold increase in energy output over that of the preceding letter. Within each such letter class, there exists a finer scaling scheme that runs from 1 to 9. Therefore, according to this labeling scheme, A1 flares are the weakest, having intensities barely above that of the quiet Sun, while X9 flares are the strongest. Typically, flares belonging to C-class and lower letter classes are considered to be weak flares. M-class flares can cause brief radio blackouts while X-class flares can cause major radiation storms that can hamper communication services, satellites and power grids. During the period of our observation, one B-class flare (B8.9 at 03 : 51 : 00 UTC) and two C-class flares (C1.3 at 01 : 51 : 00 UTC and C3.4 at 05 : 37 : 00 UTC, both from the active region with NOAA number 12149) were reported to occur on the Sun. A type-III solar burst was also reported to occur at 01 : 25 : 00 UTC.

The data were collected in a loop cycling from 79.36 MHz to 232.96 MHz in five steps of 30.72 MHz each, spending 4 minutes at each observing band. The entire 30.72 MHz DS bandwidth is composed of 24 coarse spectral channels spanning 1.28 MHz each. Each coarse spectral channel is further comprised of 32 fine spectral channels, each 40 kHz wide. The time resolution of the DS is 0.5 seconds. The data collected are then processed using two independent methods for performing separate non-imaging and imaging studies of the small-scale features of interest. These methods are described in sections 2.2 and 2.3 respectively.

2.2 Automated non-imaging study of features

2.2.1 Preprocessing

The response of a two-element interferometer to an incoming radiation field is described in terms of the crosscorrelation function between the two elements of the interferometer. If V_i and V_j are the voltages received at tiles i and j, the crosscorrelation C_{ij} measured between tiles i and j is given by :

$$C_{ij} = G_i G_j^* V_i V_j^* \tag{2.1}$$

where G_i and G_j are the complex gains of tiles i and j respectively. In order to remove the contribution of the gains of the tiles, it is convenient to normalize the crosscorrelations as follows:

$$r_{N,ij} = \frac{C_{ij}}{\sqrt{C_{ii}C_{jj}}} \tag{2.2}$$

where $r_{N,ij}$ is the normalized crosscorrelation between tiles i and j. From Eq. 2.1 and 2.2, $r_{N,ij} \propto \frac{G_i G_j^*}{\sqrt{G_i G_i^* G_j G_j^*}}$ and hence, the normalized crosscorrelations are independent of the antenna-based gains upto a phase factor.

Figure 2.1a shows a sample MWA DS of normalized crosscorrelations measured between tiles labeled “Tile011MWA” and “Tile021MWA”. The features of interest appear as short-lived, narrow-band vertical streaks against a spectrally varying broadband background continuum. In order to arrive at estimates of the energy content of these features, it is necessary to perform flux calibration of the DS. For this purpose, the flux calibration technique developed by Oberoi et al. (2016)[18] and Sharma et al. (2016)[19] has been employed. This technique provides us with reliable estimates of solar flux densities ($S_\odot$) by accounting for known contributions from the sky, receiver and ground pickup noise to the system temperature. Estimates of the sky contribution to the system temperature are obtained using the Haslam et al. 408 MHz all-sky map [20] scaled with a spectral index of 2.55[21], as a sky model. Estimates of the receiver temperature and the ground pickup temperature are arrived at using a mix of laboratory and field measurements. The requirement of keeping the Sun unresolved for the application of this flux calibration technique restricts us to using short baselines only. For the purpose of this non-imaging work, only data corresponding to one such baseline of physical length 23.7 m between tiles labeled “Tile011MWA” and “Tile021MWA” are used. Furthermore, the analysis presented in this work is carried out only for data collected in the XX polarization mode; that for the YY polarization is exactly analogous. The outputs of the flux calibration technique form the inputs for our automated wavelet-based, non-imaging study. Figure 2.1b depicts a flux-calibrated version of the DS shown in Fig. 2.1a.

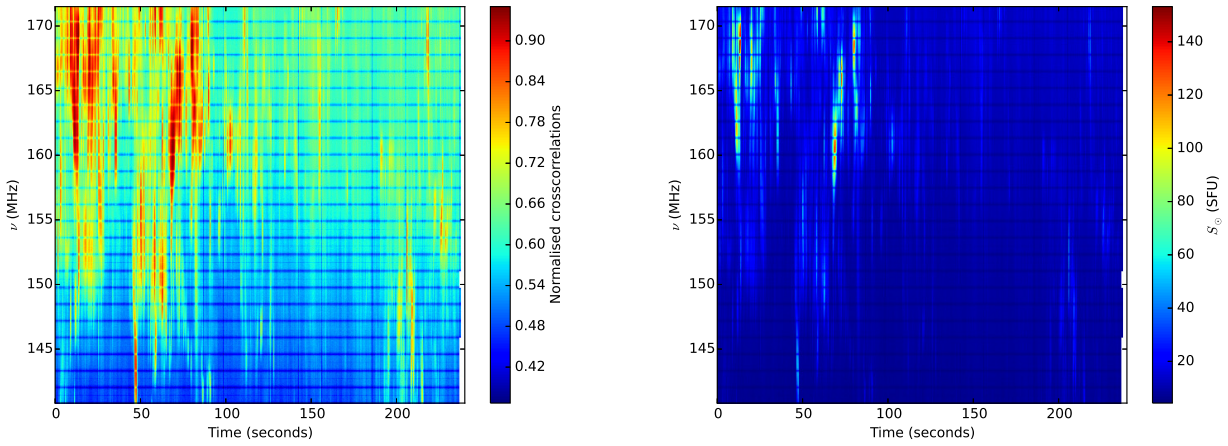

(a) **(b)**

Figure 2.1: (a): A sample MWA DS of normalized cross-correlations. (b): Flux-calibrated version of the same DS. In Fig. 2.1a, 2.1a and other DS shown in this work, the observing frequency (ν) is plotted along the vertical axis, while the time elapsed since the start of the DS is plotted along the horizontal axis. The color axes in Fig. 2.1a and 2.1a are in units of normalized crosscorrelations and solar flux densities ($S_\odot$, measured in SFU) respectively. [22]

2.2.2 Removal of instrumental artifacts

The horizontal features seen in the DS shown in Fig. 2.1a and 2.1b are artifacts arising from poor instrumental response at coarse spectral channel edges. The DS is cleaned of these artifacts by performing linear interpolation across the systematics-affected channels. As the artifacts located at the very ends of the DS bandwidth cannot be corrected through interpolation, these channels are simply discarded. Data recording glitches can sometimes affect data recorded during the first and last few seconds of an observing run. To alleviate this issue, we routinely discard the first 3 seconds and the last 4.5 seconds of data. Occasional contamination of the DS by RFI is corrected through manual RFI flagging followed by linear interpolation across RFI-affected segments of the DS. Figure 2.2a shows a version of Fig. 2.1b that is free of instrumental artifacts.

2.2.3 Background subtraction

As seen from Fig, 2.1a, the solar radiation can be considered as a superposition of the sporadic, non-thermal features on a smooth, spectrally varying, broadband background continuum. Since spectral variations associated with this broadband continuum can distort the appearance of features in the DS and hide the true shape of their spectral profiles, it is, therefore, necessary to disentangle spectral variations in the background continuum from that associated with the features of interest.

As the day of our observations was marked by medium levels of solar activity, it is reason-

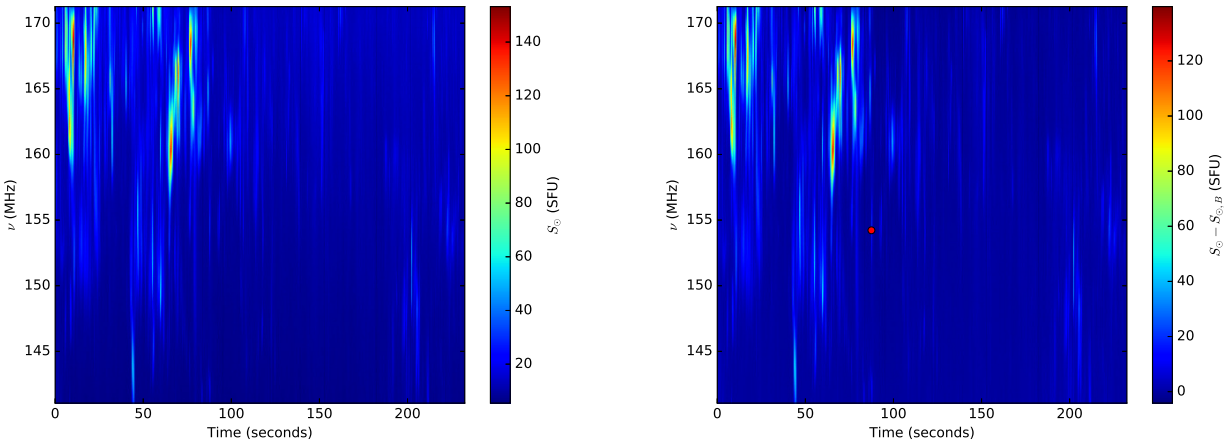

(a) **(b)**

Figure 2.2: (a): An instrumental artifact-free version of the flux-calibrated DS shown in Fig. 2.1b. (b): Background-subtracted version of the DS shown in Fig. 2.2a. The small-scale features of interest can be easily recognized in this processed DS. We note that these features also overlap in many instances. One feature that appears to be relatively isolated from the others is marked by a red circle in Fig. 2.2b. While solar flux densities ($S_\odot$) are plotted along the color axis in Fig. 2.2a, the color axes in Fig. 2.2b and other background-subtracted DS shown in this work represent background-subtracted flux densities ($S_\odot - S_{\odot,B}$). [22]

able to expect that the quiet Sun emission forms the dominant component of the background continuum in our data. We find the temporal variations of the background continuum to be negligible over the time duration of an individual DS, i.e., 4 minutes. This then allows us to neglect the time dependence of the background continuum and treat it as a function of frequency alone. As the flux densities of the weakest features in our data are only a small fraction of that of the background, an accurate and robust means of determining and subtracting out the background continuum emission is required.

In this work, the Gaussian Mixtures Model (GMM) technique provided by the Python package Scikit-Learn [23]is employed to determine the background flux density ($S_{\odot,B}$) as a function of frequency. As the background continuum is expected to vary smoothly as a function of frequency, the entire DS is divided into contiguous groups of 4 fine spectral channels each. Data belonging to each group are then separately passed through the GMM routine which decomposes these data as a sum of Gaussians. As there exists no unique way of decomposing a given function as a sum of Gaussians, the Bayesian Information Criterion (BIC) [24] is used to determine the optimum number of Gaussians required to fit the data. This criterion computes the optimal number of Gaussians required in a model to best fit the data through maximization of the overlap integral between the model and the data subject to a penalty that increases with an increase in the number of free parameters involved in the model.

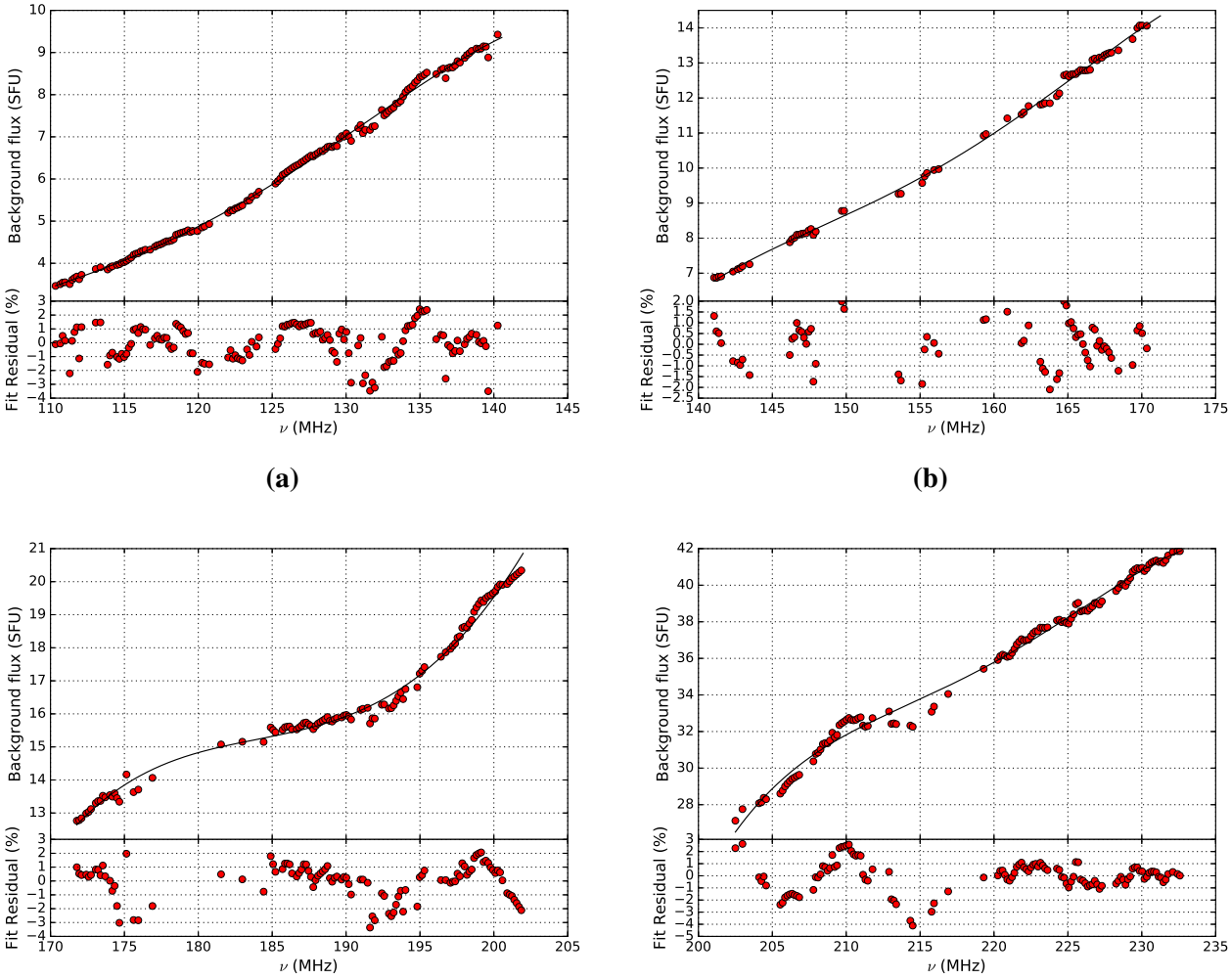

Figure 2.3: Quartic polynomial fits to the spectral trend in the background continuum and the residuals to the fits. The 4 panels corresponds to 4 different data sets having frequency ranges: (a) $110.34 - 140.54$ MHz, (b) $141.06 - 171.26$ MHz, (c) $171.78 - 201.98$ MHz, and (d) $202.5 - 232.7$ MHz. In each panel, the top sub-panel shows the polynomial fit, while the bottom sub-panel shows the departure of the best fit from the data in percentage units. [22]

Since the thermal quiet Sun emission forms the baseline solar flux level on top of which non-thermal features are detected, it is reasonable to assume that the Gaussian representing the background continuum must be the one with lowest mean and highest weight. For every group of 4 fine spectral channels, the mean value of this Gaussian is then noted as the background flux density ($S_{GMM}(\nu)$) at its respective central frequency. Presence of frequent, strong features that outshine the background can sometimes degrade our ability to arrive at an estimate of the background flux density at every observing frequency in the DS. Fortunately, our observations were taken on a day with medium solar activity levels, thus, allowing for the use of GMM to estimate the background flux density at several frequencies in most data sets.

The background flux density is then estimated across the entire DS bandwidth by fitting its large-scale smooth spectral trend with a quartic polynomial ($S_{fit}(\nu)$). This quartic polynomial is then subtracted from the DS in order to obtain a version of the DS containing the features of interest alone. Figure 2.2b depicts a background-subtracted version of the DS shown in Fig. 2.2a. The suitability of a quartic polynomial to fit spectral variations in the background flux density can be quantified by computing the residual percentage between $S_{fit}(\nu)$ and $S_{GMM}(\nu)$ at those frequencies (indicated by the red circles in the plots shown on the top sub-panels in Fig. 2.3) where $S_{GMM}(\nu)$ has been estimated. This residual percentage is given by:

$$\text{Residual } \%(\nu) = \frac{S_{GMM}(\nu) - S_{fit}(\nu)}{S_{GMM}(\nu)} \times 100\% \tag{2.3}$$

Figure 2.3 depicts the quartic polynomial fits to the estimated background continuum flux density for a few DS used in our study. According to the plots shown on the lower sub-panels in Fig. 2.3, a quartic polynomial is adequate to fit the observed spectral trend in the background flux density to within a mean absolute error of 3-4%.

2.2.4 Wavelet-based feature detection

Continuous Wavelet Transform (CWT) provides a natural way of obtaining a time-frequency representation of a non-stationary signal. In our work, the non-stationary signal is the background-subtracted DS containing the small-scale features of interest. The effectiveness of CWT at reliably picking up such features from the DS relies on the choice of a suitable 2D mother wavelet and is maximized for a mother wavelet that closely matches the shape of the spectral and temporal profiles of these features.

Choice of mother wavelet

From Fig. 2.2b, it can be seen that while there do exist features that appear isolated in the DS, several of them tend to bunch together in the DS. This leads to multiple overlaps of their spectral and temporal profiles. Figures 2.4a and 2.4b show the spectral and temporal profiles, respectively, of a relatively isolated feature marked by a red circle in the DS shown in Fig. 2.2b. A close look at such isolated features reveals a characteristic smooth, unimodal nature to their spectral and temporal profiles. Assuming that each atomic feature in the DS possesses smooth, unimodal spectral and temporal profiles, any multi-modal spectral or temporal distribution of flux densities in the DS can be considered to be a superposition of contributions from constituent unimodal distributions. This allows for a 2D Ricker wavelet to be chosen as a suitable mother wavelet for CWT. Measured in pixel units, the small-scale features of interest are extremely anisotropic, having axial ratios of about 10-50. In order to best match features of this nature, a variable separable version of a 2D Ricker wavelet which is a product of two 1D Ricker wavelets (also called the Mexican Hat Wavelet) has been used as the mother wavelet. The analytical form of this mother wavelet is:

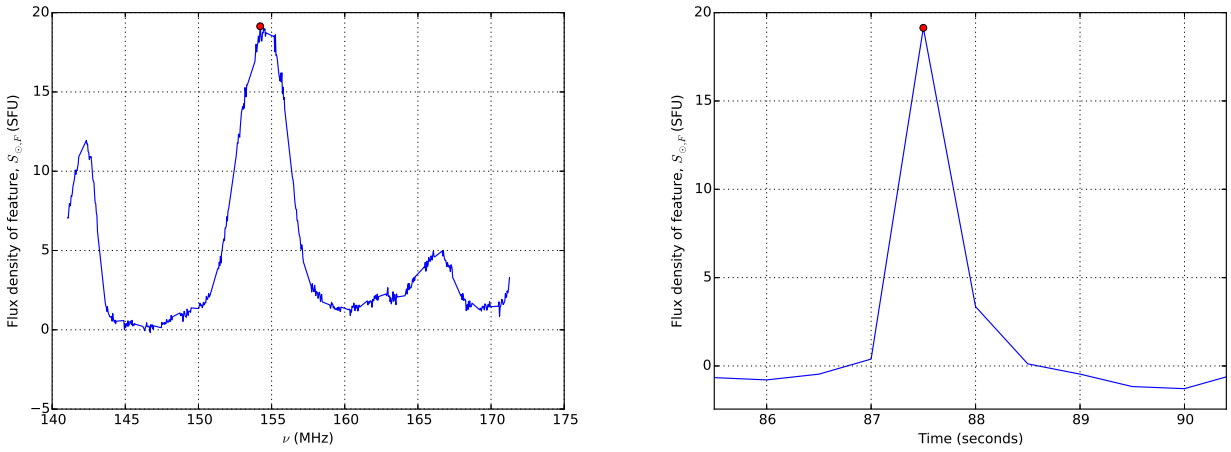

(a) **(b)**

Figure 2.4: (a): Spectral profile of the feature marked by a red circle in the DS shown in Fig. 2.2b. (b): Temporal profile of the same feature[22]

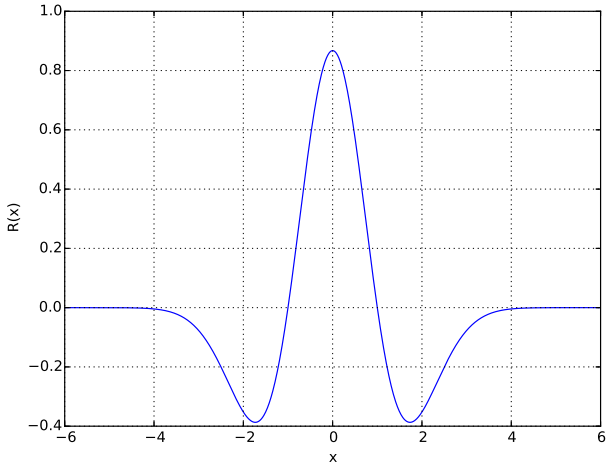

Figure 2.5: Profile of a 1D Ricker wavelet of unit scale.

$$R(t,\nu) = R(t)R(\nu) = \frac{4}{3\sqrt{\pi}}\left((1-t^2)e^{-\frac{t^2}{2}}\right)\left((1-\nu^2)e^{-\frac{\nu^2}{2}}\right) \tag{2.4}$$

where $R(t)$ and $R(\nu)$ are 1D Ricker wavelets along the time and frequency axes of the DS respectively. From this mother wavelet, scaled 2D Ricker wavelets are constructed according to the prescription given in [25] as follows :

$$R_{s_t,s_\nu,\tau_t,\tau_\nu}(t,\nu) = R_{s_t,\tau_t}(t)R_{s_\nu,\tau_\nu}(\nu) = \frac{1}{\sqrt{s_t s_\nu}}R\left(\frac{t-\tau_t}{s_t},\frac{\nu-\tau_\nu}{s_\nu}\right) \tag{2.5}$$

Here, $R_{s_t,\tau_t}(t)$ is a version of $R(t)$ that has been translated by time τ_t and scaled by a factor s_t, having dimensions of time. Similarly, $R_{s_\nu,\tau_\nu}(\nu)$ is a translated and scaled version of $R(\nu)$. Thus, the scaled 2D Ricker wavelets are versions of the mother wavelet that have been indepen-

dently scaled along the time and frequency axes. They are, hence, a suitable choice to match the anisotropy of the small-scale features of interest. The shape of a 1D Ricker wavelet of unit scale is shown in Fig. 2.5. Note that the peak of this wavelet is located at the origin and its scale equals half the support of its positive lobe. Therefore, the peak of a scaled 2D Ricker wavelet is located at $(t,\nu) = (\tau_t,\tau_\nu))$. The scales s_t and s_ν then correspond to half the support of its positive lobe along the time and frequency axes respectively. The negative lobes of the 2D Ricker wavelet are required to ensure that it has a zero mean [25].

Using the scaled wavelets, the wavelet coefficients of the DS are defined as follows:

$$\gamma(s_t,s_\nu,\tau_t,\tau_\nu) = \iint_{\nu,t} DS(t,\nu) R_{s_t,s_\nu,\tau_t,\tau_\nu}(t,\nu)\mathrm{dt}\,\mathrm{d}\nu \tag{2.6}$$

$\gamma(s_t,s_\nu,\tau_t,\tau_\nu)$ measures the degree of overlap between $R_{s_t,s_\nu,\tau_t,\tau_\nu}(t,\nu)$ and the DS, and is maximized at the locations of features with temporal and spectral spans matching the scales s_t and s_ν respectively. Thus, the 2D Ricker wavelet serves as a peak and support detection filter. This then enables us to determine the peak flux densities as well as the temporal and spectral extents of features in the DS. As τ_t and τ_ν still refer to a specific time and frequency in the DS, for the sake of convenience, we shall denote the wavelet coefficients $\gamma(s_t,s_\nu,\tau_t,\tau_\nu)$ by $\gamma(s_t,s_\nu,t,\nu)$.

Construction of a composite matrix

As 2D CWT introduces two additional degrees of freedom through transformation from a 2D DS to a 4D wavelet coefficient space, a large number of the wavelet coefficients computed for a given DS carry redundant information. The non-orthogonality of set of scaled Ricker wavelets further preserves this redundancy. This redundancy in $\gamma(s_t,s_\nu,t,\nu)$ together with the zero mean property of the 2D Ricker wavelet can be then exploited to reconstruct the DS using a basis different from the set of scaled Ricker wavelets. Here, we choose to reconstruct the DS using a basis of $\delta-$functions. Applying the 1D reconstruction formula given in [26] and extending it to the 2D scenario here, a composite matrix, $A(t,\nu)$, of wavelet coefficients that exactly reconstructs the DS, barring a constant normalization factor, is given by:

$$A(t,\nu) = \sum_{s_\nu>0}\sum_{s_t>0} \frac{\gamma(s_t,s_\nu,t,\nu)}{\sqrt{s_t s_\nu}} \tag{2.7}$$

As the wavelet coefficients are nothing but a convolution of the DS with the scaled wavelets, $A(t,\nu)$ is expected to be a smooth reconstruction of the DS. Local maxima in $A(t,\nu)$ should then correspond to peaks of features in the DS. However, there exist two issues with using $A(t,\nu)$ for feature identification. At small scales, our measurements are dominated by noise. As Eq. 2.7 involves a sum over all scales, it attempts to incorporate the measurement noise in $A(t,\nu)$. Furthermore, bunching of features leading to overlapping of spectral and temporal profiles of features can degrade the ability of CWT to distinguish between two closely spaced

features at large scales. It is, hence, necessary to work using an intermediate range of scales which enables us to capture all relevant details of features while avoiding the influence of the intrinsic measurement noise at small scales and feature overlapping at large scales. A suitable composite matrix $M(t,\nu)$ using an intermediate range of scales, is therefore, constructed using the following expression:

$$M(t,\nu) = \sum_{s_\nu=s_{\nu,lower}}^{s_{\nu,upper}} \sum_{s_t=s_{t,lower}}^{s_{t,upper}} \frac{\gamma(s_t,s_\nu,t,\nu)}{\sqrt{s_t s_\nu}} \tag{2.8}$$

Along the time domain, the features of interest exist at the time resolution of the data, forcing us to set $s_{t,lower}$ to 0.5 seconds. Careful visual inspection of a large number of DS revealed the presence of very few features with bandwidths less than 0.5 MHz. This leads us to a choice 0.5 MHz for $s_{\nu,lower}$. Again, guided by meticulous visual inspection of several DS, we set $s_{t,upper}$ to 3 seconds and $s_{\nu,upper}$ to 5 MHz in order to equip ourselves with the ability to detect atomic features present within a bunch without any compromise in the capability to detect long-lived or broadband features. The values selected for $s_{t,upper}$ and $s_{\nu,upper}$, in fact, enable us to reconstruct features having spectral and temporal extents as large as 26.04 MHz and 15 seconds respectively. Using these choices of the scales involved in Eq. 2.8, $M(t,\nu)$ is computed. Local maxima detected in $M(t,\nu)$ then correspond to the locations of peaks of features in the DS. Figures 2.6a and 2.6b demonstrate the ability of CWT to resolve atomic features present in a bunch despite overlaps in their spectral and temporal profiles.

Fig. 2.6a shows a comparison of a spectral slice taken from the DS with its corresponding slice take from $M(t,\nu)$. In this slice, three features are detected as local maxima of the $M(t,\nu)$ profile, Let us consider one of these detected features, say, the one marked with a red circle in Fig. 2.6a. We find the spectral extent of this feature to be matched well by the distance between the local minima in the $M(t,\nu)$ profile that straddle its peak. The same holds true for other detected features in this spectral slice. The distance between these local extrema is then taken as the spectral extent of the feature. The lower extremum is taken to be start frequency (ν_{start}) of the feature.

We find that the temporal extent and start time (t_{start}) of a feature can also be estimated similarly. This is illustrated explicitly in Fig. 2.6b which shows a temporal slice containing many feature detections. The peak of one feature detected in this slice is marked with a yellow circle for the purpose of aiding a visual comparison similar to that done for the feature marked in Fig. 2.6a.

In order to arrive at estimates of a quantity similar to the half power width of feature along the frequency and time axes, we define the spectral and temporal widths of a feature respec-

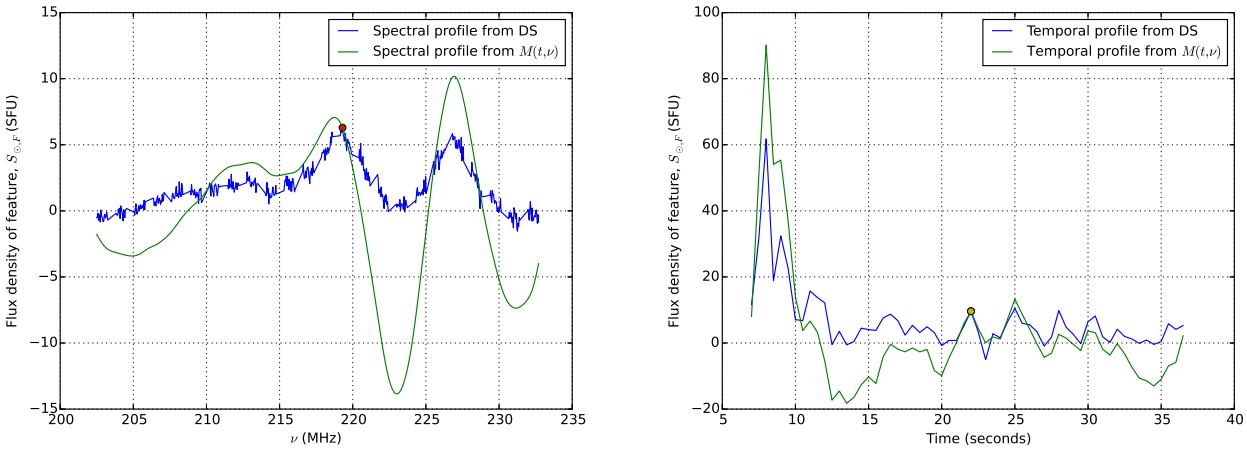

(a) **(b)**

Figure 2.6: (a) A spectral slice taken from both the DS (blue) and $M(t,\nu)$ (green). The $M(t,\nu)$ profile has three local maxima, indicating the three feature detections in this slice. The DS peak of one such detected feature is marked by a red circle. (b) A time slice taken from both the DS (blue) and $M(t,\nu)$ (green). The local maxima of $M(t,\nu)$ match closely with their DS counterparts. Of the many features detected in this slice, the peak of one such feature is marked with a yellow circle.[22]

tively as:

$$\Delta\nu = 0.5 \times \text{Spectral extent of feature}$$
$$\Delta t = 0.5 \times \text{Temporal extent of feature.}$$

For quantification of any symmetry present in the spectral profile of a feature with peak frequency ν, we define a spectral symmetry parameter as follows:

$$\chi_\nu = \frac{\nu - \nu_{start}}{2\Delta\nu} \tag{2.9}$$

χ_ν takes values in the range from 0 to 1. A value of 0.5 for χ_ν suggests a spectral profile which is symmetric about the peak frequency ν. Departures of χ_ν from 0.5 are indicative of any skewness present in the spectral profile of a feature. The temporal symmetry parameter (χ_t) of a feature is similarly defined.

2.2.5 Correction of peaks

As seen from Fig. 2.6a, peaks of features detected from $M(t,\nu)$ do not always coincide with their DS counterparts. From all the features detected across all DS used in our study, we find that the $M(t,\nu)$ peak of a feature, on an average, is offset from its corresponding DS peak by 0.16 seconds along time and 0.57 MHz along frequency. Since the $M(t,\nu)$ peaks lie close to their corresponding DS peaks, this discrepancy is easily corrected by first growing a region around the $M(t,\nu)$ peak and then identifying the true DS peak within this region. Starting from

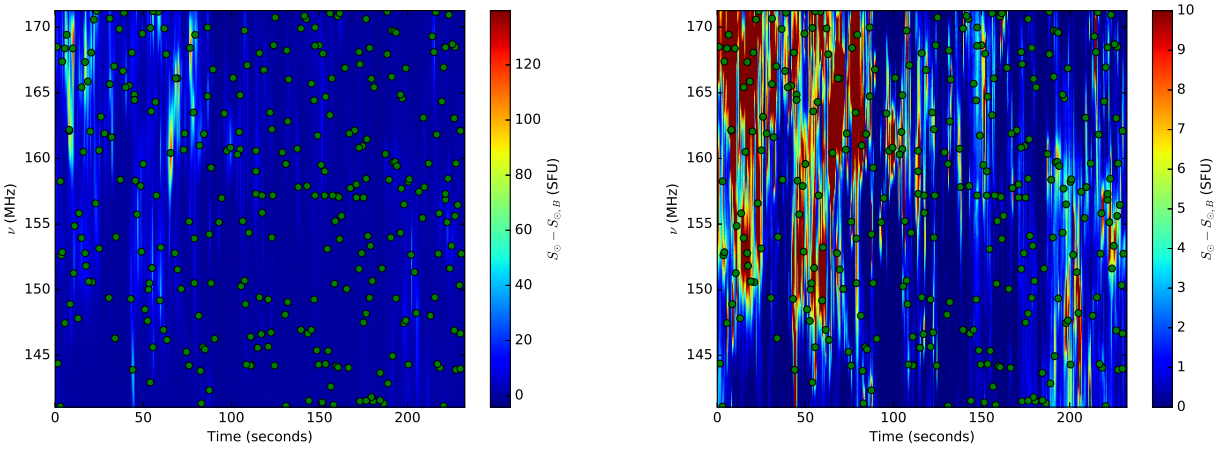

Figure 2.7: Background-subtracted DS (same as that in Fig. 2.2b) showing peaks (green circles) of features detected using the CWT pipeline. The right panel differs from the left panel only in the color bar range. While the left panel illustrates the efficiency of the CWT pipeline to pick up bright features, the right panel reveals its success at detecting weak emission features as well. [22]

a $M(t,\nu)$ peak as a seed, the admissibility criterion used to grow a region S is that the wavelet coefficient of the neighboring pixel under consideration is within a minimum threshold (T) percentage of the peak wavelet coefficient. This region growing algorithm terminates when no more pixels on the boundary of S satisfy this criterion. Since $M(t,\nu)$ is only an approximation to the DS, it reproduces the spectral and temporal profiles of a feature only within a small neighborhood of its peak. Therefore, a value of T as high as 95% has been chosen in order to ensure that all pixels enclosed within region S actually belong to the feature.

2.2.6 Elimination of false detections

Since $M(t,\nu)$ only approximates the DS, it is likely to contain peaks which lack a DS counterpart. We consider a $M(t,\nu)$ peak to be a real feature only if it has a DS counterpart. In order to weed out false peak detections, the RMS flux density ($\sigma(\nu)$) is computed over quiet patches of the background-subtracted DS as a function of frequency. A Signal-to-Noise Ratio (SNR) is then estimated for every feature by taking the ratio of its peak flux density to the RMS flux density at its peak frequency ν. Through scrupulous visual examination of the spectral and temporal profiles of all detected peaks using figures similar to Fig. 2.6, we find that false detections constitute about 24% of the total number of detected peaks. Nearly 26% of the detected peaks have peak flux densities, $S_{\odot,P} < 5\sigma$. Furthermore, all false detections are found to satisfy the $S_{\odot,P} < 5\sigma$ criterion. Hence, in order to eliminate false peak detections, we reject all peaks with peak flux density, $S_{\odot,P} < 5\sigma$.

Figure 2.7 depicts the locations of all peaks detected using our automated wavelet-based approach. In order to estimate the efficiency of this technique, 8 laypersons (BS-MS students

not involved in this work) were presented with plots of different background-subtracted DS (similar to Fig. 2.7), and requested to mark out false positives and false negatives. In this experiment, one DS which was previously visually inspected in detail during the development of the CWT pipeline was used as the control sample. This control DS was distributed to all laypersons in order to account for random person-to-person variations. According to the estimates of the laypersons, the automated wavelet-based algorithm successfully recognizes features from the DS with a zero false positive rate and a false negative rate of about 4-6%. A total of 14,177 features were detected across 67 DS used in this study. Note that while the wavelet-based approach developed here is tuned to MWA data, the technique itself is in fact quite general and can be easily applied to DS collected from other observing instruments as well.

2.3 Imaging study of features

2.3.1 Theory of Radio Imaging

Visibilities (autocorrelations and crosscorrelations) constitute the fundamental measurements made by an interferometer. For a two-element interferometer with antenna elements located at $\mathbf{r_1}$ and $\mathbf{r_2}$, the measured visibilities are a function of the baseline vector, $\mathbf{b} = \mathbf{r_1} - \mathbf{r_2}$. In radio astronomy, it is often convenient to represent $\mathbf{b}$ in terms of the wavelength (λ) as $\mathbf{b} = \lambda(u,v,w)$. Here, u, v and w define a rectangular coordinate system on the ground with w pointing in the direction from the antenna elements towards the source. This direction is uniquely defined for a distant point source in the far-field approximation, i.e., when the rays of light from the source can be assumed to arrive parallel to each other at the antenna elements. This approximation often holds true due to the large distances of astronomical sources from the Earth, when compared to baseline lengths. The coordinates u and v lie in a plane perpendicular to w, and point towards the local east and the local north respectively. Similar to the ground coordinate system, another coordinate system defined and commonly used in radio astronomy is the sky coordinate system. This coordinate system is a version of the ground coordinate system that is translated along the w axis and is centered at the location of the source on the celestial sphere[27], which is assumed to be at infinity. The coordinates of a point in this coordinate system are specified in terms of the direction cosines l, m and n measured with respect to the coordinates axes (axis parallel to u, axis parallel to v and the w axis respectively). Since l, m and n are direction cosines, they are not independent of each other but are related by the equation: $l^2+m^2+n^2=1$.

The Van Cittert-Zernike theorem relates the intensity distribution $\mathscr{I}_\nu(l,m)$ of a source in the sky at frequency ν to its monochromatic visibilities $V_\nu(u,v,w)$ and is given by[27]:

$$V_\nu(u,v,w) = \int_{-\infty}^{\infty}\int_{-\infty}^{\infty} \mathscr{A}_\nu(l,m)\mathscr{I}_\nu(l,m) e^{-2\pi i[ul+vm+w(\sqrt{1-l^2-m^2}-1)]} \frac{\mathrm{d}l\ \mathrm{d}m}{\sqrt{1-l^2-m^2}} \qquad (2.10)$$

Here, $\mathscr{A}_\nu(l,m)$ is the normalized power pattern of an antenna element. Equation 2.10 assumes

$\mathscr{A}_\nu(l,m)$ to be the same for all antenna elements. Since the primary beam of an antenna element typically confines our observations to a narrow field of view, $n = \sqrt{1-l^2-m^2} \simeq 1$. Under this condition, Eq. 2.10 then reduces to the following 2D Fourier transform relation:

$$V_\nu(u,v) = \int_{-\infty}^{\infty}\int_{-\infty}^{\infty} \mathscr{A}_\nu(l,m)\mathscr{I}_\nu(l,m)e^{-2\pi i[ul+vm]}\mathrm{d}l\ \mathrm{d}m \tag{2.11}$$

This relation can also be obtained from Eq. 2.10 when $w = 0$, i.e., when all baselines are coplanar and lie in a plane perpendicular to the direction to the source. The modified brightness distribution, $\mathscr{A}_\nu(l,m)\mathscr{I}_\nu(l,m)$ can, thus, be obtained by taking the 2D inverse Fourier transform of $V_\nu(u,v)$. $\mathscr{I}_\nu(l,m)$ is then recovered from $\mathscr{A}_\nu(l,m)\mathscr{I}_\nu(l,m)$ by performing a primary beam correction [27] to account for $\mathscr{A}_\nu(l,m)$. For the sake of convenience, let us call the modified brightness distribution as the image intensity distribution $I_\nu(l,m)$. Though Eq. 2.11 suggests that one can arrive at $I_\nu(l,m)$ by simply computing the 2D Fourier transform of the observed visibilities, practically there exist complications due to a number of factors not accounted for in Eq. 2.11.

Need for calibration

In general, the observed visibilities ($\tilde{V}_{ij}$) measured between antenna elements i and j of a two-element interferometer can differ significantly from the true visibilities (V_{ij}) for a variety of reasons. These are usually associated with propagation effects in the Earth's atmosphere (troposphere and ionosphere) and instrumental effects. The most dominant of these effects is the effective gain of the signal path, all the way from the first low-noise-amplifier to the analog-to-digital converter in the internal array system. Amongst the set of effects associated with radio wave propagation through the Earth's atmosphere, ionospheric effects are usually the most pronounced at the low radio frequencies at which the MWA operates. Ionospheric scintillations can cause rapid changes in instrumental gain amplitudes over a short period of time. For two radio waves propagating through the ionosphere, the excess phase shift introduced by the slowly varying, large-scale refractive index gradients in the ionosphere scales with the wavelength of radiation as λ^2. Owing to the 2D Fourier transform relation (Eq. 2.11) between the true visibilities and the source brightness distribution, failure to account for visibility phase drifts produced by the ionosphere could lead to the source wandering away by a few arcmin. or more. An additional ionospheric propagation effect on instrumental gain phases is Faraday rotation which gives rise to an excess phase shift between the two orthogonal polarizations of the received radiation. Other effects associated with propagation through the Earth's atmosphere include non-dispersive signal refraction in the troposphere and signal attenuation due to atmospheric opacity. Antenna pointing errors, timing errors and delays associated with signal propagation through the instrument cabling are a few other instrumental effects that can lead to errors in visibility measurements[27].

The intent behind visibility calibration is to recover the true visibilities from the observed visibilities. For a well-engineered array, all instrumental responses can be described in terms of its constituent antenna-based responses with negligible baseline-based errors. For such well-designed systems, the observed visibilities are typically a linear function of the true visibilities and are given by:

$$\tilde{V}_{ij}(\nu,t) = G_i(\nu,t)G_j^*(\nu,t)V_{ij}(\nu,t) \tag{2.12}$$

where G_i and G_j are the complex gains of antenna elements i and j respectively. These gains are, in general, a function of both frequency and time. Since frequency-dependent gain fluctuations of an antenna element are often uncorrelated with its temporal gain fluctuations, it is convenient to factor G_i as : $G_i(\nu,t) = g_i(t)B_i(\nu)$.

To perform visibility calibration, one usually observes a strong calibrator source which is near the radio source of interest in the sky and whose visibilities are reasonably well-known. Observations of such a calibrator at a time close to the intended observing period for the source of interest then enable us to accurately correct for excess ionospheric phase shifts and determine the complex antenna-based gains[27]. For this purpose, the measured visibilities of the calibrator are compared with a model containing its true complex visibilities. From this comparison, the complex factors $g_i(t)$ and $B_i(\nu)$ required to scale the observed visibilities to the true visibilities are determined. In literature, the calibrations performed to determine $g_i(t)$ and $B_i(\nu)$ are termed separately and are referred to as the gain calibration and the bandpass calibration respectively.

Dirty beam and its deconvolution from dirty image

Equation 2.11 assumes knowledge of $V_\nu(u,v)$ at all points in the $u-v$ plane. However, owing to practical considerations, it is not feasible to design arrays with complete $u-v$ coverage. In such a case, the visibility function is discretely sampled at only a few points in the $u-v$ plane. Let us define a sampling function $S(u,v)$ that equals unity at those locations in the $u-v$ plane for which the data exists and zero elsewhere. One can then compute the 2D Fourier transform of $S(u,v)V_\nu(u,v)$, commonly called the "dirty image", as follows:

$$I_\nu^D(l,m) = \int_{-\infty}^{\infty}\int_{-\infty}^{\infty} S(u,v)V_\nu(u,v)e^{2\pi i[ul+vm]}\mathrm{d}u\ \mathrm{d}v = I_\nu * B \tag{2.13}$$

Here, $B(l,m)$ is the 2D Fourier transform of $S(u,v)$ and is called the point spread function (PSF) or the dirty beam. Equation 2.13 then tells us that the dirty image is the convolution of the true image intensity distribution with the PSF. In practice, one would, therefore, need to deconvolve the PSF from the dirty image in order to arrive at the true intensity distribution.

A technique commonly used by radio astronomers for performing this deconvolution is the CLEAN algorithm[27]. This algorithm employs an iterative scheme that constructs a model

of a source by assuming it to be comprised of a large number of point sources. While several variations of the CLEAN algorithm[27] exist, the basic CLEAN algorithm functions by first identifying the position of the pixel with the highest intensity (I^D_{max}) in the dirty image. It then subtracts from the dirty image at the location of this pixel, a PSF multiplied by I^D_{max} and a damping factor γ (also called the loop gain). The strength and position of the subtracted point source is recorded in a model. This constitutes a single iteration of the CLEAN algorithm. The algorithm then proceeds to further subtract point sources from the dirty image in successive iterations until the highest intensity in the residual image drops below a certain user-defined threshold. The CLEAN algorithm can also be forced to terminate by specifying the maximum number of iterations allowed. At the end of all iterations, the accumulated point source model is convolved with a 2D Gaussian CLEAN beam to obtain a CLEAN image. The residual image is then added to the CLEAN image to obtain the final image returned by the algorithm.

2.3.2 Data selection, calibration and imaging

For performing imaging studies of the features of interest, we work with the visibilities corresponding to only 1 of the 67 solar DS analyzed in the non-imaging work. These visibilities span a duration of 4 minutes, stretching from 02 : 20 : 02 UTC to 02 : 24 : 02 UTC. This time span corresponds to a period during which no X-ray flares or major radio bursts were reported to occur on the Sun (refer Sec. 2.1). The solar visibilities cover a bandwidth of 30.72 MHz, ranging from 140.80 MHz to 171.52 MHz. The calibrator source observed as part of this imaging study was the radio galaxy Centaurus A (CenA). CenA is a strong, extended radio source, the structure of which is accurately known from independent high resolution observations. The calibrator observation was taken between 10 : 05 : 12 UTC and 10 : 07 : 04 UTC on August 31, 2014, approximately 7.75 hours after our solar observation. The calibrator visibilities cover the frequency range from 139.52 MHz to 170.24 MHz. As this frequency range is offset from that of the solar data by 1.28 MHz, we discard the upper 1.28 MHz (last coarse spectral channel) of the solar data and work with its remaining 29.44 MHz bandwidth for which we have corresponding calibrator visibilities. In this imaging work, only visibilities collected in the XX polarization mode have been analyzed. All imaging tasks were executed using tools defined in the "Common Astronomical Software Applications" (CASA) [28]software package.

Prior to calibration, we first flag data in the systematics-affected channels and time slices (refer to Sec. 2.2.2) for both the solar and calibrator measurement sets. Figure 2.8 shows the visibilities from the calibrator observation plotted as a function of the baseline length measured in wavelengths. A sharp, narrow peak can be seen in Fig. 2.8 for $\sqrt{u^2+v^2} \leq 40$. This sharp peak represents the large angular scale diffuse galactic background emission (synchrotron emission from the interstellar medium) picked up by the baselines. As we are interested in utilizing only the visibilities corresponding to CenA for performing the calibration, we exclude all visibilities picked up by baselines having length less than 40λ from our analysis. Further-

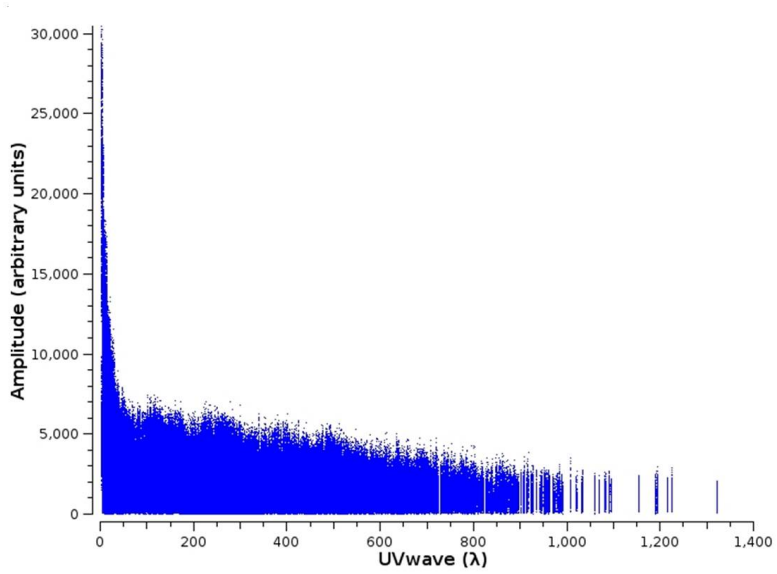

Figure 2.8: Plot of the visibility amplitudes from the calibrator data versus baseline length (UVwave = $\sqrt{u^2+v^2}$) measured in wavelengths.

more, since we require only the visibilities corresponding to the Sun for imaging it, we discard visibilities picked up by these baselines for the solar data as well.

Over the short durations of calibrator and solar observations being considered here, 2 min. and 4 min. respectively, the instrumental antenna-based gains remain constant. Ignoring effects of ionospheric scintillations, the ionospheric propagation effects appear primarily as antenna-dependent phases in instrumental gains and carry a λ^2 dependence. The small footprint of the MWA implies that to first order, these effects show up as positional shifts in the image plane. The variability of the ionospheric phases depends on the state of the ionosphere. At the mid-latitude site of the MWA, ionospheric variability is lower than that at higher latitudes or close to the equator. We, hence, neglect the temporal variations of the antenna-based gains and perform only bandpass calibration on the calibrator data. At a given frequency, the observed calibrator visibilities, integrated across the entire observing duration, are compared with their corresponding true visibilities stored in a model. This comparison is performed separately for each tile and for every observing frequency in order to estimate the complex gains $B_i(\nu)$.

Delays associated with signal propagation through cables used in the array are also, in general, a function of frequency. For the MWA, these residual uncorrected delays are typically very small ($\sim 1-10$ ns). Since these instrumental delays typically remain fixed over the short time spans of our individual observations, their frequency-dependent contributions to the complex gains then get absorbed in the computed bandpass calibration solutions.

As the Sun is an extremely bright radio source, typically an attenuator is introduced into the system electronics for solar observations alone. Introduction of the attenuator causes the gain

amplitudes for our solar observation to differ significantly from that estimated from our calibrator observation. In addition, owing to changes in the ionospheric weather and the thermal responses of the tiles, the gain phase solutions can drift significantly in the intervening long time span between our calibrator and solar observations. Furthermore, the antenna-based gains are, in general, direction-dependent quantities. In local coordinates, the altitude and azimuth of our calibrator were 53.6^{o} and 233.1^{o} respectively. On the other hand, during our solar observation, the Sun was located at an altitude of 47.9^{o} and an azimuth of 45.0^{o}. As the directions to the Sun and CenA are quite different, the gain solutions corresponding to them also differ significantly. We, therefore, need to arrive at fresh estimates of the antenna-based gains for our solar data. For this purpose, we estimate the gain amplitude and phase solutions for our solar data separately using two different methods.

We perform a relative calibration to estimate the gain amplitude solutions directly from the solar data. Relative calibration ensures that each MWA tile is calibrated with respect to every other tile. For a given frequency, we take the gain amplitude of tile i to be the square root of the minimum autocorrelation (minimum taken across time) picked by the tile at that frequency. If V_i is the voltage received at tile i with complex gain B_i, the autocorrelation (C_{ii}) measured by the tile equals $|B_i V_i|^2$. For the MWA, the minimum ($V_{i,min}$) of the voltage picked up by a tile i across time at a given frequency ν is not found to not vary significantly from tile to tile. Therefore, the spectral variation of the square root of the minimum autocorrelation, $\sqrt{(C_{ii})_{min}}$, is a reflection of the bandshape of $|B_i|$. Figure 2.9 shows the bandshape of the gain amplitude solutions estimated using the "minimum autocorrelation" criterion for two different tiles. The amplitude calibration performed here only ensures that for every pair of tiles i and j, $|B_i(\nu)|$ and $|B_j(\nu)|$ are relatively calibrated. We set the absolute scale of our calibration later during the image flux calibration stage which is described in Sec. 2.3.3.

Though our calibrator observations were taken about 8 hours later than our solar observations, we find the visibility phase drifts in the intervening time to be small enough that they are still able to make the array stay coherent. This provides us with a meaningful starting position for performing self-calibration[27] to improve our antenna gain phase estimates. As the Sun is a powerful radio source, a model derived from its image can be used to improve the gain phase solutions and thereby, refine its image. For this purpose, the bandpass phase solutions derived from the calibrator data and the gain amplitude solutions obtained from the solar autocorrelations are first applied on the uncalibrated solar visibilities to arrive at the corrected solar visibilities. A dirty image of the Sun is then made and cleaned using the CLEAN algorithm. The new gain phase solutions are arrived at by comparing the corrected solar visibilities with those stored in the accumulated point source model returned by CLEAN. These new gain phase solutions are then applied on the solar data to arrive at the true solar visibilities. Ideally, this self-calibration procedure needs to be repeated separately for each observing frequency. How-

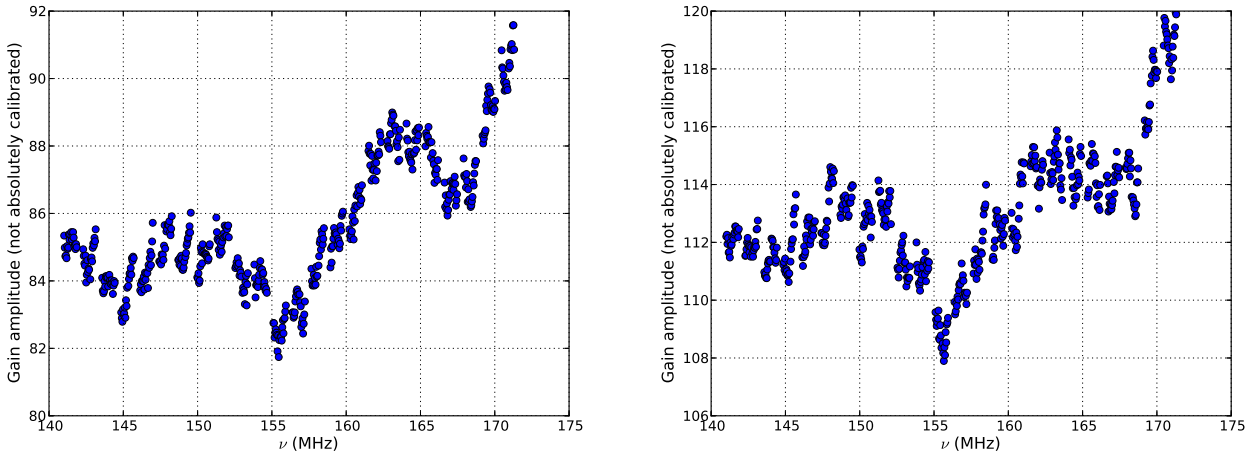

(a) **(b)**

Figure 2.9: Gain amplitude solutions estimated directly from the solar data using the minimum autocorrelation criterion for tiles labeled (a) : Tile017MWA and (b) : Tile035MWA.

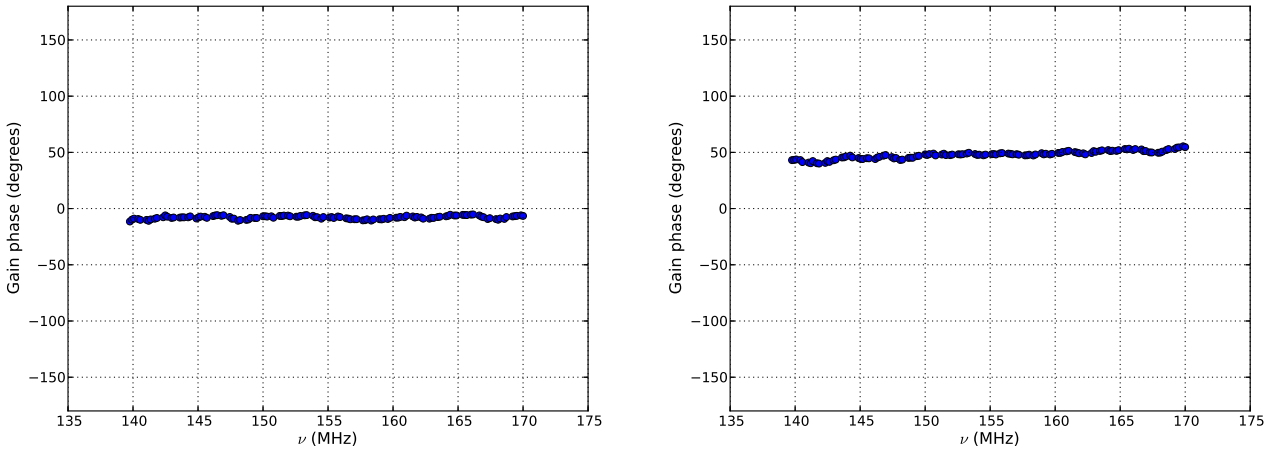

(a) **(b)**

Figure 2.10: Bandpass phase solutions estimated from the calibrator data for tiles labeled (a) : Tile017MWA and (b) : Tile035MWA.

ever, from Fig. 2.10, we note that bandpass phase solutions derived from the calibrator data are remarkably flat over the entire bandwidth. This simplifies our work and allows us to get away with performing self-calibration to determine the new gain phase solution at just one frequency. To first order, this new gain phase solution can then be uniformly applied to correct the solar visibilities across all observing frequencies.

Following the application of the bandpass phase solutions from the calibrator and the now computed complex gain solutions from the solar data, dirty images of the Sun are made. These dirty images are then CLEANed to yield the final solar images having dynamic ranges (equiv-

alently called SNR) of about $200-230$.

2.3.3 Flux calibration and estimation of brightness temperature

Though we have now obtained solar images with sufficiently high dynamic range, the image intensity scale still remains uncalibrated. This is because our solar visibility amplitudes were initially uncalibrated. As there exists a rectangular patch R in the DS corresponding to each solar image I, the flux calibration technique applied to the DS in Sec. 2.2.1 can then be transferred to the solar images. To do so, we choose a certain threshold contour of image intensity with level I_{thresh} in an image I and estimate the total image flux S enclosed within this contour. This flux S is then scaled to the mean flux contained in the corresponding patch R in the DS. I_{thresh} is typically defined as the minimum value of the image intensity for which the intensity contour levels in the image capture emission from the solar disk as a single extended source with no discontinuous blotches. Through meticulous visual investigations of several solar images, the value for I_{thresh} determined to be the most suitable for our solar data was : $I_{thresh} = 12\sigma$ where σ is the RMS noise on the image.

Having flux-calibrated the solar images, we can now estimate the brightness temperature of sources in the solar images using the Rayleigh-Jeans law as follows:

$$T_b = \frac{\lambda^2 S}{2k_b\Omega} \tag{2.14}$$

where S is the flux density (in SI units) and Ω is the solid angle of the restoring CLEAN beam. For a Gaussian restoring beam with half power bandwidth θ_{HPBW} :

$$\Omega = \frac{\pi\theta^2_{HPBW}}{4\ \ln 2} \tag{2.15}$$

Inserting the above expression for Ω into Eq. 2.14 and expressing λ in cm, θ_{HPBW} in arcseconds and S in mJy/beam, we have:

$$T_b = 1.36\frac{\lambda^2 S}{\theta^2_{HPBW}} \tag{2.16}$$

2.3.4 Tracking source sizes and source motions on the solar disk

The wavelet-based algorithm reveals the presence of 213 features in the sole solar DS used for this imaging study. Of these, 30 features lie in the last coarse spectral channel of the DS for which calibrator data is not available (refer to section 2.3.2). Therefore, excluding these features, brightness temperature images of the remaining 183 features were made. The temporal profile of each feature in the DS is characterized by two parameters, viz., the time t at which it peaks in the DS and its temporal span Δt. With the knowledge of these parameters from the wavelet-based work, three images at the peak frequency ν were made for every feature corresponding to times $t-\Delta t$ (just before the feature), t (during the feature) and $t+\Delta t$ (right after

the feature). Thus, a total of 549 images were analyzed in this work. All images were made using a time averaging of 0.5 seconds and a frequency averaging of 0.28 MHz. Each of these images show the presence of one or more compact sources, the brightness of which is found to vary in the "before", "during" and "after" images (refer to Sec. 3.5) of features.

Characterization of the sources of these features on the solar disk is the major aim of our imaging study. It is expected that source motions and morphologies contain information about the nature, locations, sizes and dynamics of the magnetic field bundles confining the electron beams which are believed to be accelerated at magnetic reconnection sites and are giving rise to the radio emission. Small jitters observed between source locations at different frequencies for the same time can be representative of density inhomogeneities in the solar corona. We find that the compact sources in our solar images are described well by a 2D elliptical Gaussian model. This provides us with a convenient way to characterize their amplitudes, locations and morphologies (refer to Sec. 3.6). Variations in the elliptical Gaussian model parameters then likely correspond to the variations in the underlying electron density inhomogeneities and / or the 3D shape of magnetic field bundles. An ability to reliably track these variations can potentially provide a completely new tool to follow the coronal magnetic field evolution in detail. A detailed investigation of this is beyond the scope of this work and hence, we simply identify and present any trends observed in source motions and morphologies without entering into a discussion about their physical interpretations.

Tracking of source locations and morphologies is performed using the CASA imfit task. This task, when applied on a dirty image of a feature, determines the locations and sizes of one or more sources (if present in the dirty image) by imposing a 2D elliptical Gaussian model to fit the source intensity distribution in the image. The parameters returned by the imfit task are the source locations, source sizes, source intensity amplitudes and the errors on the 2D elliptical Gaussian fit. While the source locations are described in terms of the source right ascension (RA) and source declination (Dec), the source sizes are quantified in terms of the lengths of the major and minor axes (measured in arcseconds) of the 2D elliptical Gaussian fit to the source shape. In astronomy, RA is usually measured in units of hours, minutes and seconds, while Dec is expressed in units of degrees and arcminutes. In addition to the source locations and sizes, imfit also returns the amplitude and position angle (measured in degrees) of the 2D Gaussian fit to the source, the position angle of the PSF, and the lengths of its major and minor axes.

Knowledge of location of sources on the solar disk allows us to search for associations with active regions from solar images taken at other wavelengths. The NASA Solar Dynamics Observatory (SDO) images the Sun with a cadence of 12 seconds at 10 different wavelengths in the EUV and X-ray band of the electromagnetic spectrum using its Atmospheric Imaging Assembly (AIA) instrument. One of the ten wavelengths tracked by AIA is the 94 Å Fe (XVIII)

emission line. This emission traces regions of the solar corona associated with solar flares. Since solar radio emission originates from the outer corona, the SDO AIA 94 Å images are the most suitable EUV images with which solar radio images can be compared in order to search for any possible correlation between phenomena operational at these wavelengths. However, we understand that the emission in the EUV and the radio wavebands are expected to arise from rather different coronal heights, and that the non-radial component of magnetic fields bundles can make it harder to make one-to-one associations between the EUV image and the radio image. In this work, we use the SDO AIA 94 Å image to hunt for possible correlations between radio sources of the features of interest and bright flaring regions in the solar corona.

Typically, all SDO AIA images are made with the convention that the Solar North Pole (SNP) is placed at the top of the image. On the other hand, a solar radio image typically has the North Celestial Pole (NCP) placed at its top. Therefore, in order to compare our radio images with an AIA image, we rotate our radio images so as to place the SNP at their top. The exact angle by which this rotation should be performed is determined from the NASA JPL HORIZONS system (`http://ssd.jpl.nasa.gov/horizons.cgi`). According to the NASA JPL solar ephemeris generated for the day of our observations, our radio images needed to be rotated by 20.79^{o} in the counter-clockwise direction about the center of the optical Sun in order to place the SNP at their top.

Chapter 3

Results

The multitude of features detected using the CWT pipeline enables us to build statistically stable distributions of their properties, in particular, their peak flux densities and morphology in the DS. Imaging studies of such features then allow us to probe the distributions of their source sizes and source locations on the solar disk. In the following sub-sections, we present distributions of various quantities of physical interest for these features.

3.1 Peak flux densities

Figure 3.1a shows the histogram of peak flux density ($S_{\odot,F}$) of features. This distribution is affected by incompleteness at low flux densities (due to instrumental sensitivity limits and use of the 5σ threshold in Sec. 2.2.6) and limited statistics at high flux densities. We, hence, choose to fit a power law to an intermediate range of flux densities where we expect the distribution to be complete. We find that a least squares power law fit to this histogram results in a power law index $\alpha = -2.23$ over the $12-155$ SFU flux density range. While the numerical value of α depends on the choice of endpoints for the power law fit, we find its value to be stable and consistently less than -2 irrespective of this choice in the $10-160$ SFU flux density range. From Fig. 3.1a, we also note that the residuals to the power law fit are manifestly non-Gaussian, implying the inadequacy of power law model to fit these data. However, the uncertainty in the best fit power law index is only about 1%, suggesting that a power law is reasonable, though sub-optimal description of the data. While we note that a polynomial in log-log space would serve as a better fit to the data, we have chosen to fit a power law here as it renders itself easily to an interesting physical interpretation from a coronal heating perspective and provides us with a point of comparison with previously published literature in this field.

The value of α obtained for the power law fit in Fig. 3.1a is intermediate between that obtained for type-I bursts ($\alpha \approx -2.9$ to -3.6) [16, 29]and type-III bursts ($\alpha \approx -1.66$ to -1.80) [17]. However, it agrees well with the estimates of α obtained in two recent studies of type-I bursts in radio noise storms ($\alpha \approx -2.5$ in [30], $\alpha \approx -2.2$ to -2.6 in [31]) observed using the Gauribidanur Radio Heliograph array. The flux range of the power law fit in Fig. 3.1a overlaps with that of the power law fits performed for type-I bursts[16]. The upper end of this flux range approaches the lower end of the flux range of similar fits performed for type-III bursts[17].

Figure 3.1b shows a 2D histogram of the peak flux densities of features plotted as a func-

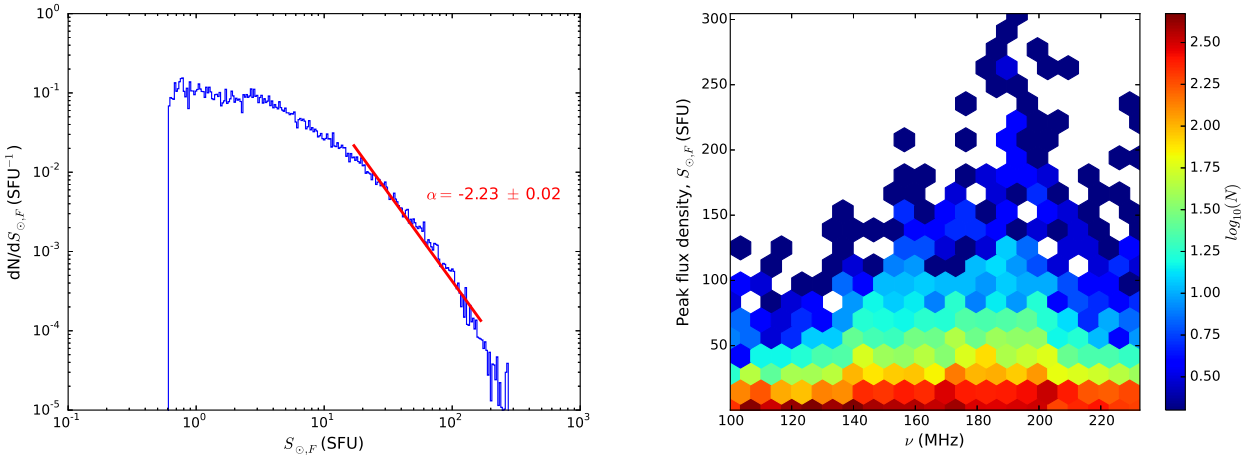

(a) **(b)**

Figure 3.1: (a): Histogram of peak flux densities on a log-log scale. (b): 2D histogram showing variation of the peak flux density with peak frequency. The color axis is in log_{10} units. [22]

tion of the peak frequency (ν). We find that the peak flux density for a majority of features is largely independent of ν. However, for a sub-population of features, we do notice a frequency-dependent variation in their peak flux density. For this sub-population, the peak flux density increases with ν from 100 MHz to 150 MHz, remains constant between 150 MHz and 200 MHz and then decreases beyond 200 MHz.

3.2 Spectral and temporal widths

Figures 3.2a and 3.2b show distributions of spectral widths ($\Delta\nu$) and temporal widths (Δt) of features respectively. Both $\Delta\nu$ and Δt follow smooth, unimodal distributions. The peak of the $\Delta\nu$ distribution lies at about $4-5$ MHz, well above the 40 kHz frequency resolution of the data. However, the Δt distribution peaks at about $1-2$ s, close to the 0.5 s time resolution of the DS. From the 2D histogram shown in Fig. 3.2c, we note that the distributions of $\Delta\nu$ and Δt arrange themselves into a single, well-formed cluster which peaks at about $4-5$ MHz and $1-2$ s. While the spectral widths of these features are nearly two order of magnitude smaller than that of type-III bursts, they are comparable to the typical bandwidths of type-I bursts[16].

Figure 3.3a shows a 2D histogram of $\Delta\nu$ and the peak frequency (ν) of features. The prominent peak and valley-like structures are artifacts arising from the finite bandwidth of observations. While valleys are present at the edges of a DS bandwidth, peaks occur at its centre. There appears to be a hint of a small increase in $\Delta\nu$ with increase in ν ($\Delta\nu/\nu \approx 0.03$).

The data, when originally collected, contained an equal number of observations at all frequency bands. While our background subtraction routine worked successfully on most data sets, the background flux density could not be determined for about 24% of the data, typically

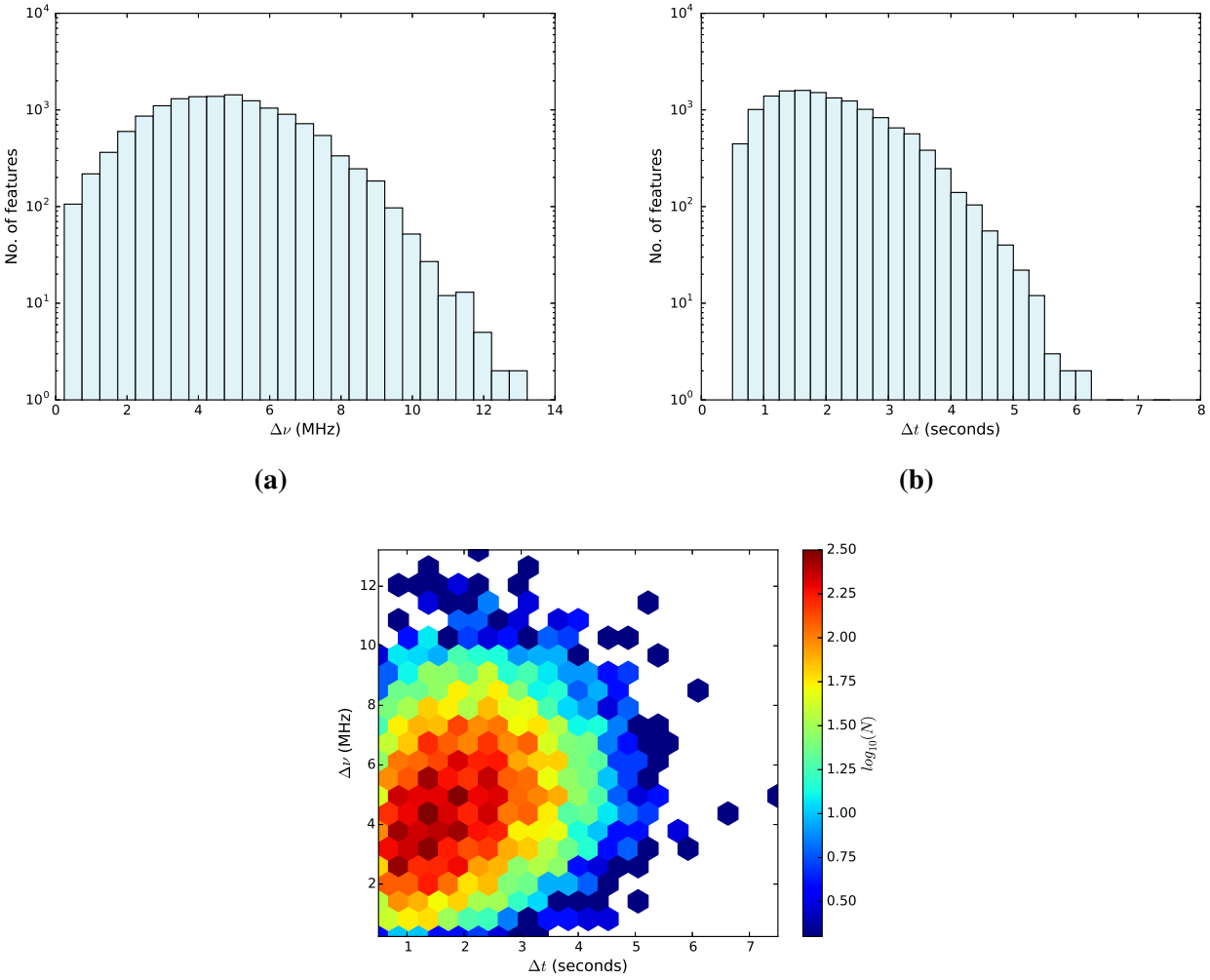

Figure 3.2: (a): Histogram of spectral widths, $\Delta\nu$. (a): Histogram of temporal widths, Δt. (c): 2D histogram of $\Delta\nu$ and Δt. The color axis is in log_{10} units. [22]

those characterized by high solar activity (corresponding to times immediately after the occurrences of the B and C-class flares). These data were then discarded from our analysis. This leads to an unequal number of observations at different frequencies and is reflected in the feature counts represented along the color axis in Fig. 3.3a. In order to arrive at the true spectral distribution of features, we estimate the feature occurrence rate per unit bandwidth as a function of frequency. From the histogram shown in Fig. 3.3b, we find that the spectral distribution of features remains largely flat between $140-210$ MHz and declines below 140 MHz. At low frequencies ($\nu \leq 140$ MHz), the background galactic emission becomes stronger while the solar emission becomes weaker[18]. This lowers the SNR of our detections and thereby, gives rise to the declining feature count rates at the low frequency end of Fig. 3.3b. As most features at these frequencies have peak flux densities $S_{\odot,F} \lesssim 10$ SFU (see Fig. 3.1b), the low SNR of feature detections at these frequencies contributes to the incompleteness at the low flux density end of the histogram shown in Fig. 3.1a.

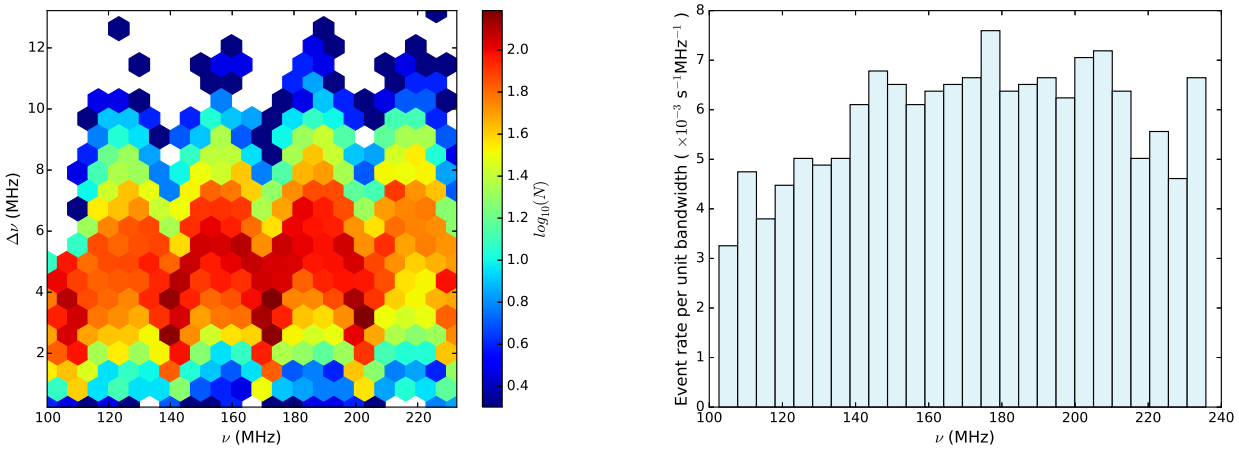

(a) **(b)**

Figure 3.3: (a): 2D histogram showing distributions of spectral widths, $\Delta\nu$ and peak frequencies, ν. The color axis is in log_{10} units. (b): Histogram showing variation of feature occurrence rate per unit bandwidth (of order 10^{-3}s^{-1}MHz^{-1}) as a function of ν. [22]

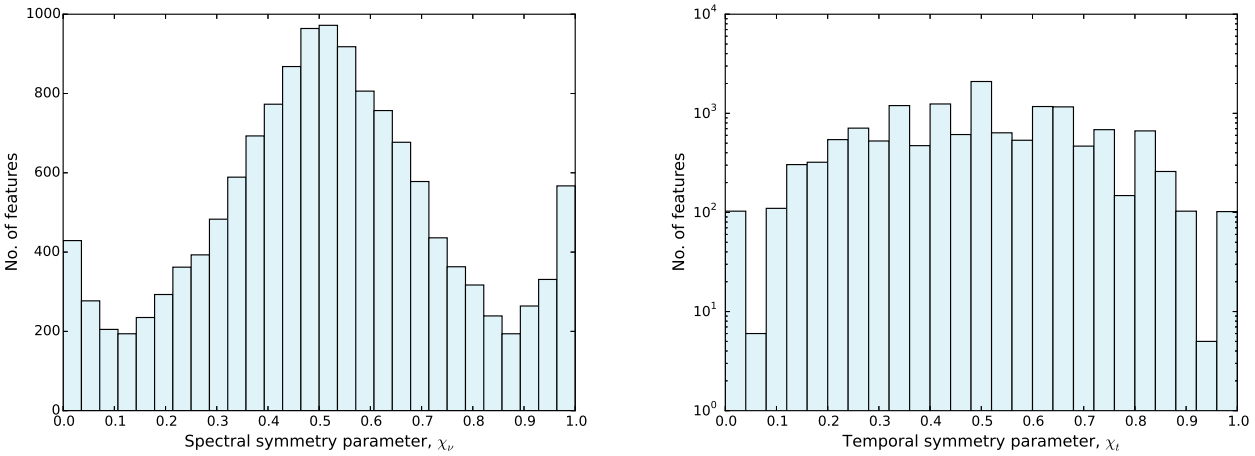

(a) **(b)**

Figure 3.4: (a): Histogram of spectral symmetry parameter, χ_ν (b): Histogram of temporal symmetry parameter, χ_t. [22]

3.3 Spectral and temporal profiles

Histograms of the spectral (χ_ν) and temporal symmetry (χ_t) parameters, shown in Fig. 3.4a and 3.4b respectively, reveal interesting findings about the nature of the spectral and temporal profiles of features. While most features possess symmetric spectral profiles, their temporal profiles display no intrinsic symmetry. The presence of features which are located close to the edges of a DS gives rise to the peaks seen at the extremes of the χ_ν and χ_t histograms.

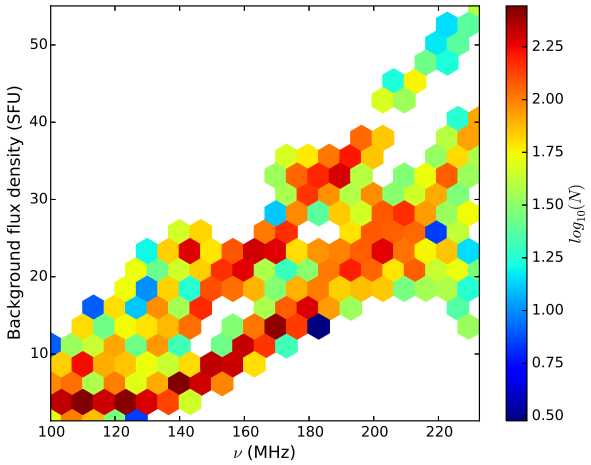

Figure 3.5: 2D histogram showing distributions of the background flux densities at the locations of features in the DS and the corresponding peak frequencies. The color axis is in log_{10} units. [22]

3.4 Background flux density at peak frequency

Figure 3.5 shows a 2D histogram of the background flux density as a function of frequency. The background continuum emission displays the expected monotonic increase with frequency due to thermal emission from the 10^6 K coronal plasma. This suggests that the quiet Sun emission forms a major component of the smooth, spectrally varying, broadband background continuum. However, according to solar observations taken by the RSTN (Radio Solar Telescope Network; `(http:/www.sws.bom.gov.au/World_Data_Centre`), the median solar flux density during our observing period was estimated to be 20 SFU at 245 MHz. As compared to this estimate, the background continuum appears to be enhanced, varying by a factor of two at all frequencies. Over the course of our observing period, the background continuum is also observed to vary significantly over a time scale of 30 minutes.

3.5 Association with active regions

Figure 3.6 shows the background-subtracted solar DS used for the imaging work. Three distinct points of interest in this DS are labeled by circular markers. Let us look at radio images corresponding to these points one by one.

The yellow circle represents a relatively "quiet point" at t = 12 s in the DS. The CLEANed image corresponding to this point is shown in Fig. 3.7a. Though this point is not associated with any feature, its image still reveals the presence of a bright, compact source. Let us label this source as "Source 1". We find Source 1 to be consistently present in the images of all feature-less regions of the DS. From Fig. 3.7a, we note that the brightness temperature (T_b) of Source 1 during feature-less regions is of order 10^7 K. There also appears to be a hint of the

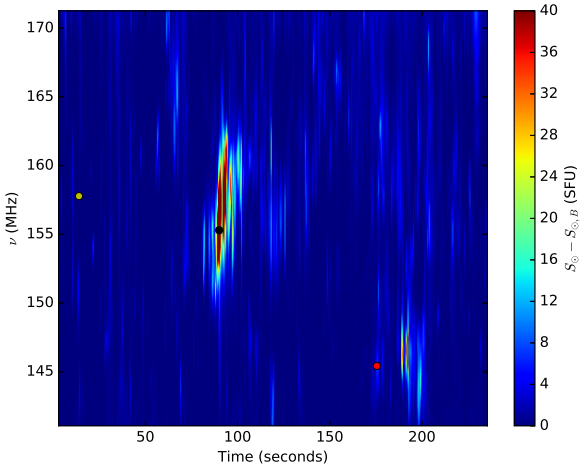

Figure 3.6: Background-subtracted DS used for imaging. The strtongest feature in this DS is marked by a black circle and is characterized by a peak flux density of 90.7 SFU. A weak feature, having a peak flux density of 7.1 SFU is marked by a red circle. The yellow circle represents a relatively quiet point in the DS. The maximum of the color bar scale has been set to 40 SFU in order to illustrate the presence of quiet data points and weak features better.

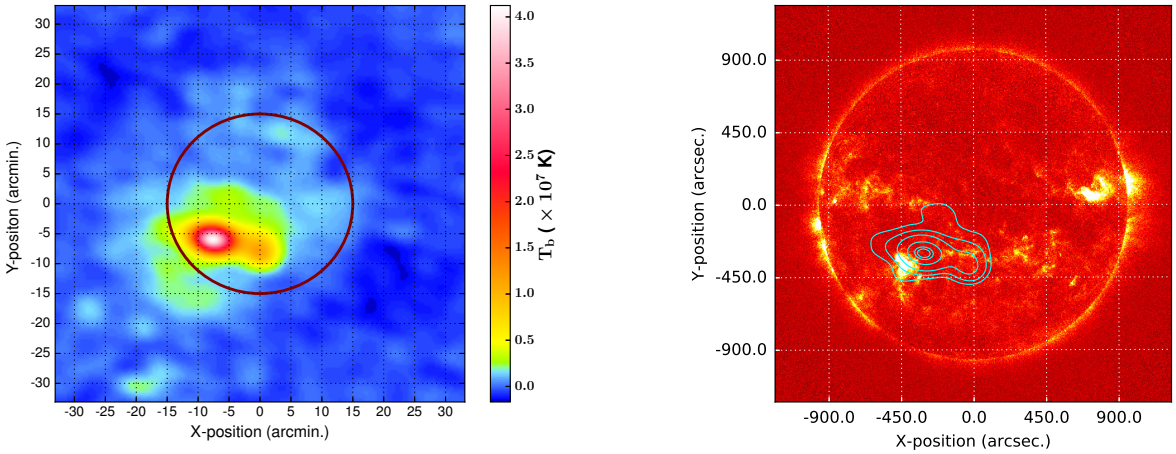

(a) **(b)**

Figure 3.7: (a): Radio image of the quiet point marked by a yellow marker in the DS shown in Fig. 3.6. The solid maroon circle in this radio image represents the optical disk of the Sun.(b): Radio contours from Fig. 3.7a overplotted on the SDO AIA 94 Å image of the Sun taken 12 seconds later. Starting from the outermost radio contour and moving inwards, the 6 plotted contour levels correspond to brightness temperatures that are respectively, 6, 10, 20, 50, 80 and 90 percent of the peak brightness temperature of the radio source shown in Fig. 3.7a.

extended quiet Sun emission from the solar disk.

Figure 3.7b displays an AIA 94 Å solar image taken at 02 : 20 : 25 UTC on the day of our observations. Radio contours from Fig. 3.7a are overplotted on this AIA image. From this figure, we find Source 1 to be associated with a bright flaring region seen at EUV wavelengths.

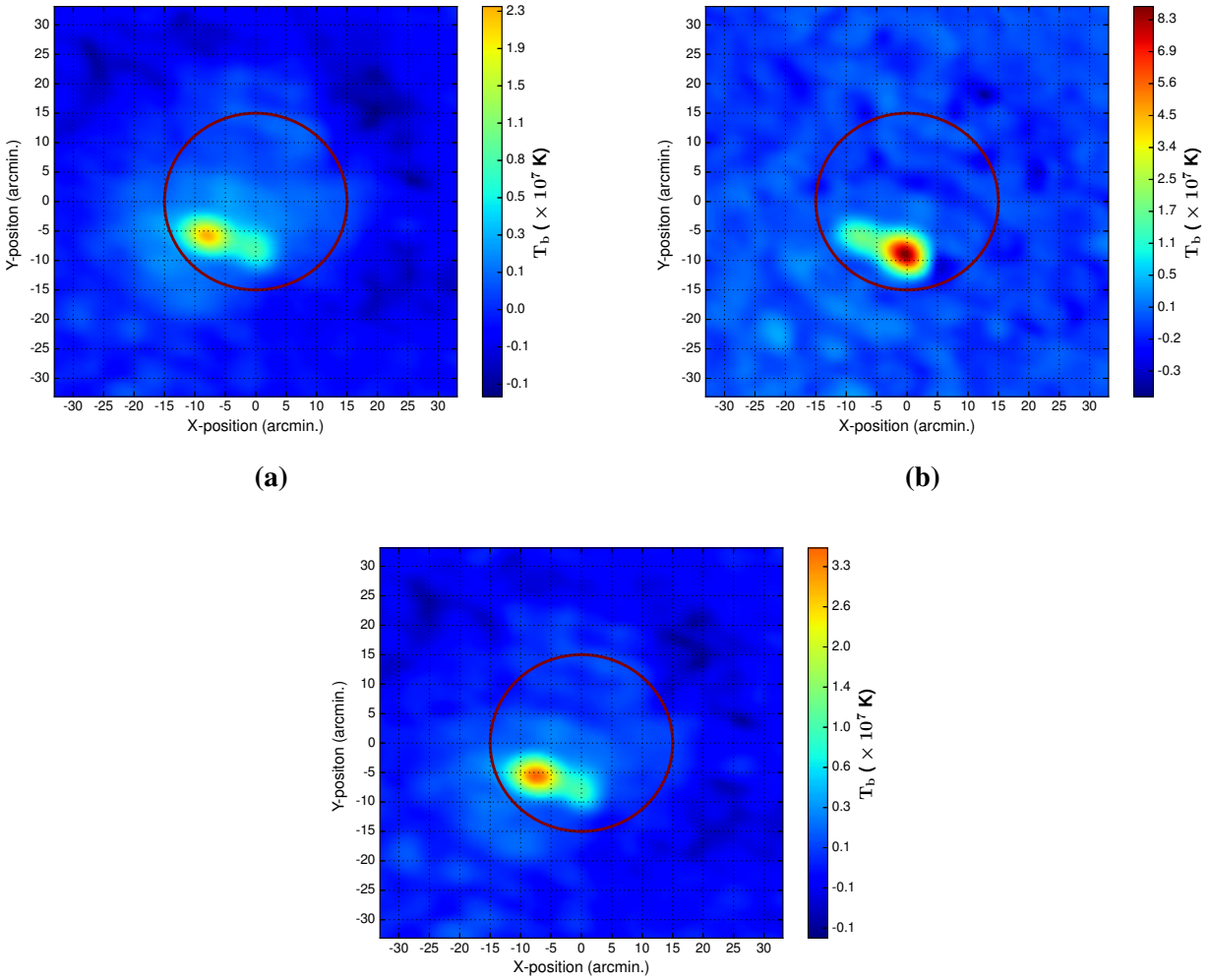

Figure 3.8: Radio images corresponding to times (a): just before, (b): during and (c): just after the occurrence of the feature marked by a red circle in the DS shown in Fig. 3.6. In each image, the solid maroon circle represents the optical disk of the Sun.

The red circle in Fig. 3.6 represents a weak feature, having a peak flux density of 7.1 SFU. Radio images corresponding to times just before, during and right after the occurrence of this feature are depicted in Fig. 3.8a, 3.8b and 3.8c respectively. The centroid of radio emission is seen to shift from Source 1 to another transient source in its vicinity during the peak of the feature. Let us label this transient source as "Source 2". Though this feature lasts for only 3 seconds in the DS, its occurrence is marked by a sharp rise in T_b from its pre-feature value of 2.4×10^7 K to a value of 9×10^7 K during the feature. After the feature, the centroid of radio emission returns back to Source 1 and the maximum T_b in the image drops to 3.6×10^7 K.

Finally, the black circle in Fig. 3.6 represents the strongest feature in the DS, with a peak flux density of 90.7 SFU. Figures 3.9a, 3.9b and 3.9c show solar radio images made just

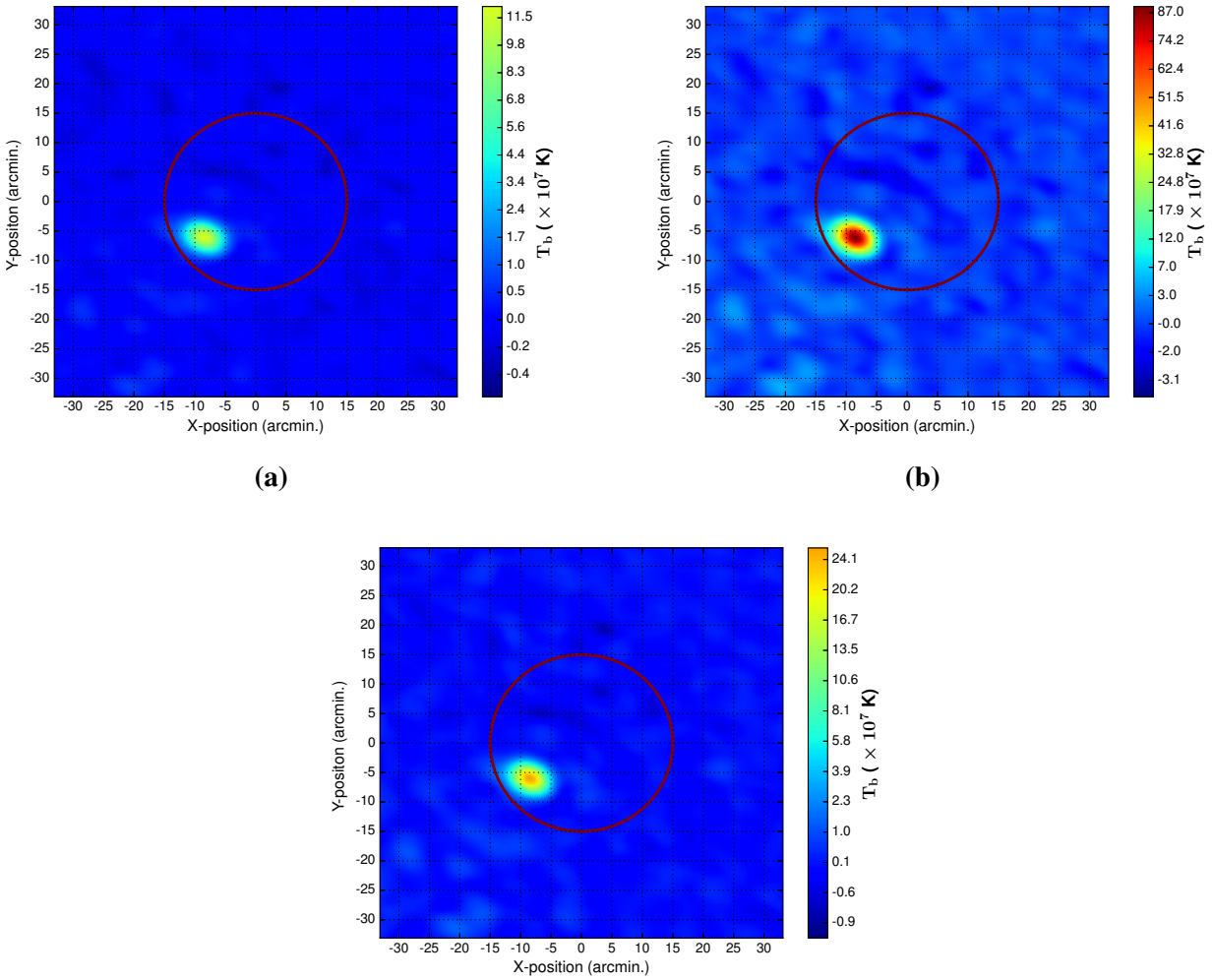

Figure 3.9: Radio images made at times (a): just before, (b): during and (c): just after the occurrence of the strong feature indicated by a black circle in Fig. 3.6. In each image, the solid maroon circle represents the optical disk of the Sun.

before, during and just after its occurrence respectively. Here, we find that the centroid of radio emission remains stationary at Source 1. However, similar to that observed for the weak feature previously discussed, the T_b of Source 1 suddenly shoots up from its pre-feature value of 1.2×10^8 K to a value of 8.9×10^8 K during the feature. After the feature, its T_b falls to 2.5×10^8 K. Through visual inspection of images of all features detected in the DS shown in Fig. 3.6, we find the two different motions displayed by the centroid of radio emission for the two features investigated here to constitute the major trends observed in source motion.

3.6 Distributions of source locations and sizes

Figure 3.10 shows the distribution of locations of Source 1 and Source 2 as a function of frequency in the RA-Dec plane. Both Source 1 and Source 2 occupy nearly fixed locations in the RA-Dec plane with a small scatter ($\approx 4-8$ s along RA axis and ≈ 1 arcmin. along Dec axis)

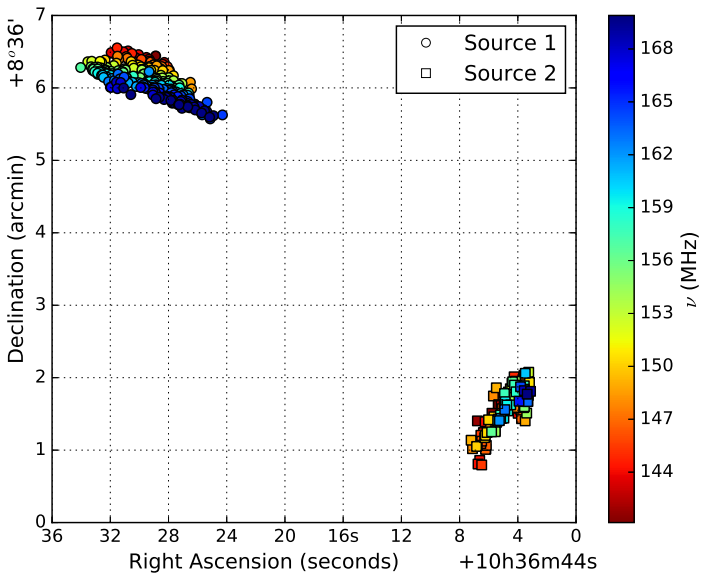

Figure 3.10: Distribution of locations of Source 1 and Source 2 as a function of frequency in the RA-Dec plane.

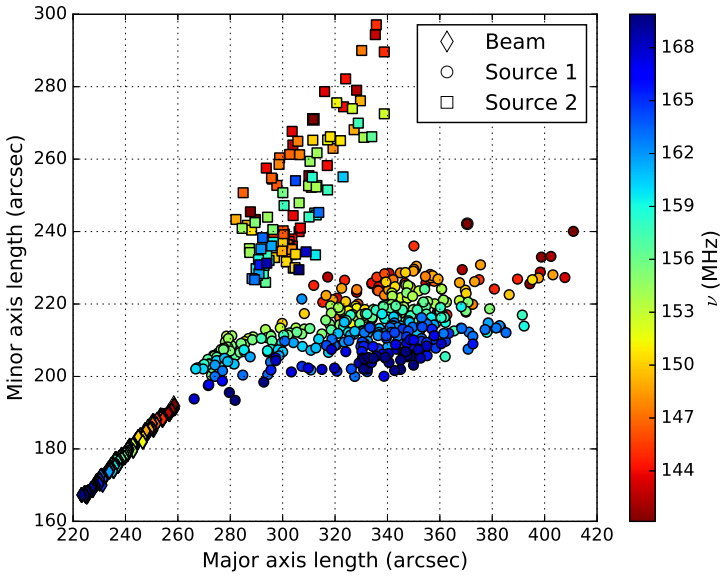

Figure 3.11: Distribution of major and minor axes lengths of Source 1, Source 2 and the PSF plotted as a function of frequency.

about their mean positions. While Source 1 seems to move towards higher declinations at lower frequencies, Source 2 shows no clear trend with frequency in the RA-Dec plane. Figure 3.11 depicts the distribution of the major and minor axes lengths of these sources as a function of frequency and compares them with the size of the PSF. We again find that points corresponding to these two sources form two distinct clusters. As the size of the PSF is determined by the resolution limit of the instrument (limit of resolution $= \lambda/b$ where b is the length of the longest

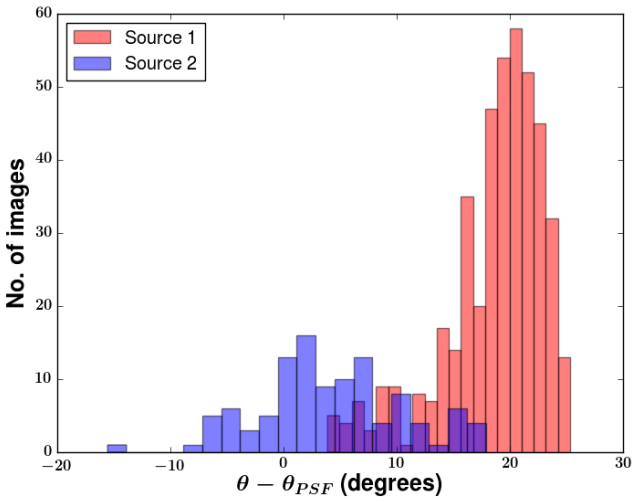

Figure 3.12: Histograms of the inclinations of Source 1 and Source 2 with respect to the PSF.

baseline), the lengths of its major and minor axes are both proportional to λ. They are, hence, expected to scale linearly with respect to each other. The PSF sizes, as shown in Fig. 3.11, display this expected behavior. While the lengths of the minor axes of the two sources of interest appear to increase with decreasing frequencies, their major axes lengths show no observable trend with frequency. Source 1 appears to be characterized by a shorter minor axis length than Source 2. However, the range of major axis lengths associated with Source 1 is greater than that for Source 2. From Fig. 3.11, we also observe that the sizes of these two sources are larger than that of the PSF, implying that both are extended sources. The clear spectral trends (see Fig. 3.10 and 3.11) observed in the source fit parameters suggest that further detailed investigations of these data could uncover more details about the emission process and geometry.

The small errors associated with the determination of the source locations (error in source RA $\approx 10^{-2}$ s, error in source Dec $\approx 10^{-2}$ arcmin), source major axes lengths (error ≈ 10 arcsec), source minor axes lengths (error ≈ 4 arcsec) and the position angle (θ) of the elliptical Gaussian fit to the source (error $\approx 1^{o} - 2^{o}$) suggest that a 2D elliptical Gaussian serves as a suitable model to fit the observed source intensity distribution. We also note that the errors on the major and minor axes lengths of the 2D Gaussian fit are very small in comparison to the median PSF size (median major axis length = 4 arcmin, median minor axis length = 3 arcmin). Thus, the 2D Gaussian fit provides us with a powerful tool to track the motion of the centroid of radio emission at scales much finer than the intrinsic resolution of the observing instrument.

3.7 Distributions of source orientations

Histograms of the orientations of the two sources of interest relative to that of the PSF are shown in Fig. 3.12. While Source 2 appears to be only slightly inclined (by about $3^{o} - 7^{o}$) with respect to the PSF major axis, Source 1 is highly inclined by about 20^{o} to the same side of the PSF major axis as Source 2.

Chapter 4

Discussion

4.1 Energies of features

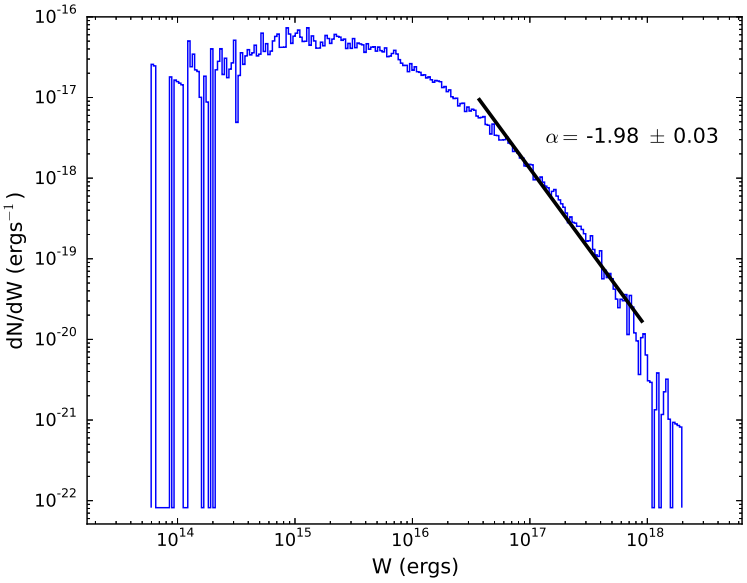

Figure 4.1: Histogram of radiated energies of features. [22]

Having estimated the peak flux densities ($S_{\odot,F}$), bandwidths ($\Delta\nu$) and durations (Δt) of the features of interest, we can obtain estimates of their radiated energy output if we know the solid angle into which radiation is emitted. Assuming isotropic emission of radiation, the total energy (W) radiated for a feature when observed from a distance $D = 1$ AU is given by: $W = 4\pi D^2 \Delta\nu \Delta t S_{\odot,F}$. As this definition of W takes into consideration only the peak flux density of a feature without accounting for any flux density reduction within its shape and assumes isotropic emission, W is an overestimate of the actual radiated feature energy. While many previous works[17, 31] use constant burst bandwidths and durations to compute W, here we have calculated W using the spectral and temporal spans that were estimated for each feature. Figure 4.1 shows a histogram of the total radiated feature energies. The typical radiated energy output associated with the features of interest is about $10^{15} - 10^{18}$ ergs. They are, hence, weaker than both type-I bursts ($W \approx 10^{21}$ ergs) [16] and type-III bursts ($W \approx 10^{18} - 10^{23}$ ergs) [17]. A least squares power law fit to the tail of this histogram yields a power law index $\alpha = -1.98$. For weak flare emissions to contribute significantly to coronal and chromospheric heating, the power law index of their flare energies must satisfy the criterion $\alpha \leq -2$ [15]. Within the uncertainty of the

fit, the features investigated here meet this criterion and can, hence, be expected to contribute to coronal and chromospheric heating in an energetically significant manner. However, though they satisfy the energy requirement for contributing to coronal heating, our imaging studies reveal that they are closely tied to active radio sources. Their spatial distributions over the solar disk, hence, do not meet the expectations from a nanoflare-based coronal heating perspective.

Theoretically, the ratio of the radiative power output from radio noise storm continua to the total power input provided to the accelerated, non-thermal electrons producing them is estimated to be $10^{-10} - 10^{-6}$[32]. Assuming this efficiency estimate, the total energy transferred to the non-thermal electrons responsible for producing the small-scale features of interest is about $10^{21} - 10^{28}$ ergs. This agrees well with known estimates of the energies ($\approx 10^{23} - 10^{26}$ ergs) associated with the accelerated, supra-thermal populations of electrons that produce radio noise storms [32, 31]. This, therefore, hints at a possible correlation between the properties of the small-scale features of interest and that of type-I bursts.

4.2 Correlation with type-I bursts

Our statistical analysis shows that the small-scale features in the MWA DS typically possess spectral and temporal spans of about $4-5$ MHz and $1-2$ seconds respectively. These numbers are comparable to the typical bandwidths ($\Delta\nu \leq 10$ MHz) and durations (Δt ~1 s) reported for type-I bursts in literature. In addition, at the time resolution of the data, the features of interest appear as stationary bursts with no detectable frequency drift rate in the DS. This finding then suggests a possibility of the detected features being weak cousins of type-I bursts. However, it is likely that they might actually possess small frequency drifts that are not measurable at the time resolution of the MWA data,

The wavelet-based analysis further reveals that these features appear to ride on a broadband, spectrally varying background continuum. From Fig. 3.5, we note that this background continuum emission varies nearly by a factor of two at all frequencies. Such large variations in the broadband background continuum over time scales as short as 30 minutes are unlikely to represent changes in the thermal quiet Sun emission from the 10^6 K solar coronal plasma. This then suggests the presence of an additional broadband continuum emission that enhances our estimated background flux densities to values greater than that expected if it were comprised of the quiet Sun emission alone. These findings, thus, closely agree with observations of type-I bursts superposed on a broadband continuum in radio noise storms.

Imaging studies of the features of interest uncover the presence of two bright, compact, extended radio sources. While one of these sources is transient and is present only during the peak of some features, the other appears to be persistently present at all times, even during feature-less regions of the DS. The observed brightness temperatures of these two sources are of

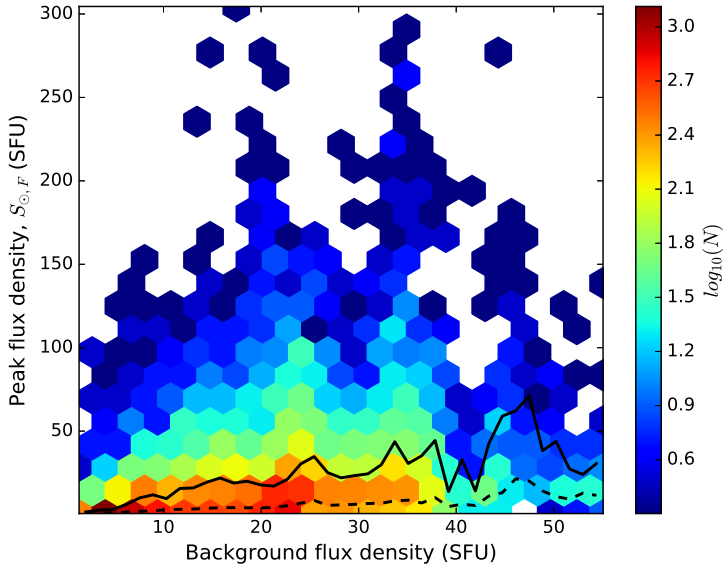

Figure 4.2: 2D histogram of the peak flux densities of features and the background flux density at their peak frequency. The color axis is in log_{10} units. The dashed and solid black lines represent respectively the first and the third quartile of the distribution of peak flux densities within a background flux density bin. [22]

order $10^7 - 10^8$ K. These brightness temperature estimates are larger than the expected physical electron temperature of 10^6 K in the solar corona. This suggests that a coherent emission mechanism is operational behind the production of these features. The presence of a bright, compact source in all radio images together with its observed association with a flaring region in the NASA SDO AIA 94 Å image strongly indicate that our data represent observations of a radio noise storm (type-I storm) with the detected features being type-I bursts embedded in the noise storm. These results then support the theory of type-I burst production proposed by Benz & Wentzel (1981)[4], and Spicer et al. (1982)[33]. This theory describes type-I bursts as observational signatures of scattered small-scale energy release events in the solar corona. The very electrons accelerated in such small-scale magnetic reconnection events might give rise to both the burst-like feature emission as well as the broadband background continuum.

Figure 4.2 shows a two-dimensional histogram of the peak flux densities of features and the background flux density at their peak frequencies. The 25th and the 75th percentiles of the distribution of peak flux densities are also plotted as a function of the background flux density and are represented by the dashed and solid black curves respectively. The first quartile of the peak flux density distribution increases from 0.76 SFU at a background flux density of 2 SFU to 10.18 SFU at a background flux density of 38 SFU. The third quartile of the peak flux density distribution grows from 1.59 SFU to 44.39 SFU over the same range of background flux densities. Noting that we are limited by statistics beyond a background flux density of 38 SFU, these trends, thus, demonstrate a tendency for an increase in the peak flux density of a

feature with an increase in the background flux density. Together with the observed variability in the background continuum, these then give rise to a possibility that the enhanced background continuum might arise from a superposition of a multitude of weak features which remain unresolved at the time resolution of our data. However, observations of such small-scale weak features with finer time resolution are required in order to understand them better.

Chapter 5

Conclusions and Outlook

We have carried out a detailed statistical characterization of the small-scale features observed in the MWA DS. Owing to their high occurrence rates of a few thousands per hour in the DS bandwidth, an automated wavelet-based technique has been developed for their recognition and subsequent parameter extraction from the DS. Individual features in the DS are found to possess smooth, unimodal spectral and temporal profiles, and a 2D Ricker wavelet is very effective at locating them. Using the CWT pipeline, a total of 14,177 features were detected from across 67 DS. With knowledge of their peak flux densities, locations in the DS, and their temporal and spectral spans, imaging and non-imaging studies were independently performed to investigate their properties.

The small-scale features of interest are characterized by typical radiated energies of about $10^{15} - 10^{18}$ ergs and are, hence, weaker than both type-I as well as type-III bursts. The distribution of their peak flux densities is well-fitted by a power law with index $\alpha = -2.23$ over the $12 - 155$ SFU flux density range. A least squares power law fit to the tail of the histogram of their radiated energies yields a power law index $\alpha = -1.98$. Within the uncertainty of this fit, $\alpha \lesssim -2$, suggesting that they could contribute to coronal and chromospheric heating in an energetically significant manner.

For these features to satisfy the expectations from a nanoflare-based theory on coronal heating, it is required that they display a lack of correlation with known active regions. However, radio imaging studies reveal each of these features to be tied to either one of two bright, compact radio sources seen on the solar disk. While one of these radio sources appears only during the occurrence of some features, the other is persistently present, even during feature-less regions of the DS. The presence of this persistent radio source together with its close association to a flaring region observed at EUV wavelengths strongly indicate that our data represent observations of a type-I storm. The detected small-scale features then correspond to weak type-I bursts embedded in this radio noise storm.

Analogous to type-I bursts, these features appear as stationary bursts in the MWA DS showing no detectable frequency drift at the time resolution of the DS. Their typical spectral and temporal spans are about $4 - 5$ MHz and $1 - 2$ seconds respectively. In addition, they also appear to ride on a variable, enhanced background continuum.

In this work, an attempt has been made to track radio source locations and morphologies using a 2D elliptical Gaussian fit. A 2D elliptical Gaussian model is found to serve as a powerful tool to probe source locations and morphologies with an accuracy much better than the intrinsic resolution of the observing instrument. The 2D elliptical Gaussian fits to the two radio sources of interest reveal that they are both extended sources of radio emission.

Radio source morphologies and locations could likely contain important information about coronal electron density inhomogeneities and the geometry of magnetic field bundles tied to the supra-thermal electron population responsible for feature production. It is hoped that this statistical, robust characterization of small-scale, non-thermal emission features shall engender interest in the theory and simulation community to model these features in order to understand them better.

References

[1] M. J. Aschwanden, *Physics of the Solar Corona : An Introduction with Problems and Solutions*, Ch. 15 : Radio Emission, pp. 637–662, (Springer-Praxis Publishing, 2006).

[2] G. B. Rybicki, A. P. Lightman, *Radiative Processes in Astrophysics*, Ch. 1 : Fundamentals of Radiative Transfer, pp. 25–26, (Wiley VCH Publishing, 2004).

[3] D. B. Melrose, *Coherent Emission*, Vol. **257** of Universal Heliophysical Processes, Proceedings of the International Astronomical Union, IAU Symposium, pp. 305–315, (2009).

[4] A. O. Benz, D. G. Wentzel, *Coronal evolution and solar type I radio bursts - an ion-acoustic wave model*, Astronomy & Astrophysics **94**, 100B (1981).

[5] N. Gopalswamy, W. T. Thompson, J. M. Davila, M. L. Kaiser, S. Yashiro, P. Mäkelä, G. Michalek, J. L. Bougeret, R. A. Howard, *Relation Between Type II Bursts and CMEs Inferred from STEREO Observations*, Solar Physics **259**, 227 (2009).

[6] H. A. S. Reid, H. Ratcliffe, *A Review of Solar Type III Radio Bursts*, The Astrophysical Journal **14**, 773–804, (2014).

[7] A. O. Benz, *Plasma Astrophysics : Kinetic Processes in Solar and Stellar Coronae*, Ch. 5 : Kinetic Plasma and Particle Beams, pp. 89–113, (Kluwer Academic Publishing, 2003).

[8] D. E. Morosan, P. T. Gallagher, P. Zucca, et al., *LOFAR tied-array imaging and spectroscopy of solar S bursts*, Astronomy & Astrophysics **580A**, 65M (2015).

[9] D. Oberoi, L. D. Matthew, I. H. Cairns, et al., *First Spectroscopic Imaging Observations of the Sun at Low Radio Frequencies with the Murchison Widefield Array Prototype*, The Astrophysical Journal **728L**, 27O (2011).

[10] S. D. T. Beltran, S. Cutchin, S. White, *A New Look at Type-III Bursts and Their Use as Coronal Diagnostics*, Solar Physics **290**, 2423T (2015).

[11] C. J. Lonsdale, R. J. Cappallo, M. F. Morales, et al., *The Murchison Widefield Array: Design Overview*, IEEE Proceedings **97**, 1497 (2009).

[12] S. J. Tingay, R. Goeke, J. D. Bowman, et al., *The Murchison Widefield Array: The Square Kilometre Array Precursor at Low Radio Frequencies*, Publications of the Astronomical Society of Australia **30**, 7T (2013).

[13] J. D. Bowman, I. H. Cairns, D. L. Kaplan, et al., *Science with the Murchison Widefield Array*, Publications of the Astronomical Society of Australia **30**, 31B (2013).

[14] E. N. Parker, *Nanoflares and the Solar X-ray Corona*, The Astrophysical Journal **330**, 474P (1988).

[15] H. S. Hudson, *Solar flares, microflares, nanoflares, and coronal heating*, Solar Physics **133**, 357H (1991).

[16] C. Mercier, G. Trottet, *Coronal Radio Bursts: A Signature of Nanoflares?*, The Astrophysical Journal **474L**, 65M (1997).

[17] P. Saint-Hilaire, N. Vilmer, A. Kerdraon, *A Decade of Solar Type III Radio Bursts observed by the NANCAY Radioheliograph 1998-2008*, The Astrophysical Journal **762**, 60S (2013).

[18] D. Oberoi, R. Sharma, A. E. E. Rogers, *Estimating solar flux density and brightness temperature at low radio frequencies using a sky brightness model*, Accepted by Solar Physics (2017).

[19] R. Sharma, D. Oberoi, et al., *Quantifying weak non-thermal solar emission at low radio frequencies*, Manuscript under preparation (2017).

[20] C. G. T. Haslam, C. J. Salter, H. Stoffel, W. E. Wilson, *A 408 MHz all-sky continuum survey. II - The atlas of contour maps*, Astronomy & Astrophysics Supplement Series **47**, 1H (1982).

[21] A. E. Guzmán, J. May, H. Alvarez, K. Maeda, *All-sky Galactic radiation at 45 MHz and spectral index between 45 and 408 MHz*, Astronomy & Astrophysics **525A**, 138G (2011).

[22] A. Suresh, R. Sharma, D. Oberoi, S. B. Das, V. Pankratius, B. Timar, C. J. Lonsdale, et al., *Wavelet-Based Characterization of Small-Scale Solar Emission Features at Low Radio Frequencies*, Submitted to The Astrophysical Journal (2016).

[23] F. Pedregosa, G. Varoquaux, A. Gramfort, V. Michel, B. Thirion, O. Grisel, M. Blondel, P. Prettenhofer, R. Weiss, V. Dubourg, J. Vanderplas, A. Passos, D. Cournapeau, M. Brucher, M. Perrot, E. Duchesnay, *Scikit-learn: Machine Learning in Python*, Journal of Machine Learning Research **12**, 2825–2830 (2011).

[24] K. P. Burnham, D. R. Anderson, *Model selection and multimodel inference: a practical information-theoretic approach*, (Springer Publications, 2002).

[25] J. P. Antoine, R. Murenzi, P. Vandergheynst, S. T. Ali, *Two-dimensional wavelets and their relatives*, (Cambridge University Press, 2004).

[26] C. Torrence, G. P. Compo, *A Practical Guide to Wavelet Analysis*, Bulletin of the American Meteorological Society **79**, 61T (1998).

[27] G. B. Taylor, C. L. Carilli, R. A. Perley, *Synthesis Imaging in Radio Astronomy II*, Vol. **180** of ASP Conference Series, pp. 11–170, (1999).

[28] J. P. McMullin, B. Waters, D. Schiebel, W. Young, K. Golap, *Astronomical Data Analysis Software and Systems XVI*, Vol. **376** of ASP Conference Series, pp. 127–131, (2007).

[29] K. Iwai, Y. Miyoshi, S. Masuda, F. Tsuchiya, A. Morioka, H. Misawa, *Spectral Structures and Their Generation Mechanisms for Solar Radio Type-I Bursts*, The Astrophysical Journal **789**, 4I (2014).

[30] V. Mugundhan, R. Ramesh, I. V. Barve, C. Kathiravan, G. V. S. Gireesh, P. Kharb, A. Misra, *Low-Frequency Radio Observations of the Solar Corona with Arcminute Angular Resolution: Implications for Coronal Turbulence and Weak Energy Releases*, The Astrophysical Journal **831**, 154 (2016).

[31] R. Ramesh, K. S. Raja, C. Kathiravan, A. S. Narayan, *Low-frequency Radio Observations of Picoflare Category Energy Releases in the Solar Atmosphere*, The Astrophysical Journal **762**, 89R (2013).

[32] P. Subramanian, P. A. Becker, *Noise storm continua: power estimates for electron acceleration*, Solar Physics **225**, 91 (2004).

[33] D. S. Spicer, A. O. Benz, J. D. Huba, *Solar type I noise storms and newly emerging magnetic flux*, Astronomy & Astrophysics **105**, 221S (1982).